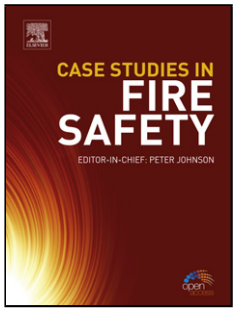

Title: Influence of hydrogen on the mechanical and fracture properties of some martensitic advanced high strength steels in simulated service conditions

Author: Jeffrey Venezuela Qingjun Zhou Qinglong Liu Mingxing Zhang Andrej Atrens

PII: S0010-938X(16)30263-3
DOI: http://dx.doi.org/doi:10.1016/j.corsci.2016.05.040
Reference: CS 6801

To appear in:

Received date: 13-1-2016
Revised date: 19-5-2016
Accepted date: 30-5-2016

Please cite this article as: Jeffrey Venezuela, Qingjun Zhou, Qinglong Liu, Mingxing Zhang, Andrej Atrens, Influence of hydrogen on the mechanical and fracture properties of some martensitic advanced high strength steels in simulated service conditions, Corrosion Science http://dx.doi.org/10.1016/j.corsci.2016.05.040

Highlights

The influence of hydrogen on four MS-AHSS was investigated in simulated service conditions.

Hydrogen had little influence on the four MS-AHSS in 3.5 wt% NaCl.

There was little influence for hydrogen-precharged MS1300 and MS1500 at substantial stress rates.

The diffusivities of hydrogen in MS980, MS1300 and MS1500 were similar.

The use of a Pt counter electrode during cathodic hydrogen charging is not recommended.

Influence of hydrogen on the mechanical and fracture properties of some martensitic advanced high strength steels in simulated service conditions

Jeffrey Venezuela[1], Qingjun Zhou[2,*], Qinglong Liu[1], Mingxing Zhang[1], Andrej Atrens[1,*]
[1] The University of Queensland, Division of Materials, School of Mining and Mechanical Engineering, St. Lucia, 4072 Australia
[*] Corresponding author, andrejs.atrens@uq.edu.au, +61 7 3365 3748,
zhouqingjun@baosteel.com, +86 21 26641807
[2] Baoshan Iron & Steel Co., Ltd, Research Institute, Shanghai, 201900,China

ABSTRACT

This work investigated the influence of hydrogen on the mechanical and fracture properties of four martensitic advanced high-strength steels in simulated service conditions: (i) immersed in 3.5 wt% NaCl solution, and (ii) at substantial applied stress rates. There was little influence of hydrogen for the four MS-AHSS in 3.5 wt% NaCl. Similarly, there was little influence of hydrogen for hydrogen-precharged MS1300 and MS1500 subjected to tensile tests at substantial stress rates. The diffusivities of hydrogen in MS980, MS1300 and MS1500 were similar. The use of a Pt counter electrode during cathodic hydrogen charging is not recommended.

Keywords: A. steel; B. SEM; Hydrogen embrittlement; XPS C. hydrogen embrittlement

1. INTRODUCTION

Martensitic advanced high strength steels (MS-AHSS) belong to a new class of steels that are used in the manufacture of lightweight, crashworthy cars [1-3]. MS-AHSS are the strongest of these AHSS, but exhibit limited ductility and formability [4]. MS-AHSS are important because of their good strength and relatively low cost [5]. MS-AHSS are used in automobiles as anti-intrusion components, such as bumper beams and reinforcements, door intrusion beams and reinforcements, windscreen upright reinforcements, and B-pillar reinforcements [1,6-8]. In each of these typical applications, under normal service, the MS-AHSS steel is subjected either to zero stress, or a constant low stress. However, there are high loading rates and high stresses under crash situations. Because of the increasing use of MS-AHSS, it is important to understand their performance under service conditions. In particular,

this study addresses the issue of hydrogen embrittlement of these steels under service conditions.

Hydrogen embrittlement (HE) is a concern for high-strength steels [9-34]. HE is caused by the interaction of the steel, hydrogen and stress. HE can result in (i) a reduction of the yield and tensile strength, (ii) subcritical crack growth, and (iii) a loss of ductility [9,10]. Alternatively, HE can cause some loss of ductility without an appreciable reduction in yield and tensile strength [35], and with no sub-critical crack growth. HE susceptibility of MS-AHSS [36-39] increases with (i) increasing strength, (ii) decreasing applied strain rate or decreasing applied stress rate, (iii) decreasing tempering temperature, (iv) the presence of large inclusions, and (v) and the presence of large second phase precipitates.

This current research builds on our previous study, using the linearly increasing stress test (LIST), on the HE susceptibility of the four MS-AHSS (MS-AHSS, MS980, MS1180, MS1300 and MS1500) [39]. The LIST [40] has been widely used to study hydrogen embrittlement (HE) and stress corrosion cracking (SCC) [12,41-50]. The LIST, shown schematically in Fig. 1, is based on a lever beam balanced on a fulcrum. On one side is the specimen. The other side of the lever beam has a moveable weight, which can be moved outwards along the lever beam at a constant rate, and subjects the specimen to a linearly increasing (engineering) stress until fracture. In the initial, elastic part of the test, the LIST is essentially identical to the constant extension rate test (CERT). Both the LIST and CERT can be used to determine the onset of yielding, or the onset of subcritical crack growth, using a potential drop technique. The LIST test is load controlled, and consequently the LIST is completed at the fracture stress when the specimen has become mechanically unstable. For tests with ductile fracture, necking of the specimen only commences at the ultimate tensile stress, when the specimen is mechanically unstable, and is undergoing ductile fracture. This ductile fracture occurs quickly. The LIST specimen can be exposed to air, or to a suitable testing solution.

Our previous study [39] showed that the HE susceptibility of the four MS-AHSS (with yield strengths in the range 880 to 1360 MPa) increased with (i) increasing strength, (ii) decreasing applied stress rate, and (iii) increasing hydrogen fugacity. Both the yield and the tensile strengths were somewhat decreased, particularly for the highest strength steels at the slowest applied stress rate, in the presence of a significant amount of hydrogen introduced by cathodic charging. The decrease in yield strength was attributed to solid solution softening by

hydrogen. The main effect of the hydrogen was to decrease ductility, facilitate the occurrence of brittle shear fracture, and cause some brittle features (e.g. intergranular and transgranular fractures) on the fracture surface, but there was no subcritical cracking.

The present paper addresses the relevance to automobile service of the prior studies of HE susceptibility of MS-AHSS. The specific issues addressed are as follows.

1. The HE susceptibility of MS-AHSS containing a hydrogen concentration typical of the manufactured steel.
2. The HE susceptibility of MS-AHSS under simulated service conditions, which would cause hydrogen to enter the steel due to the corrosion of the steel in service.
3. The changes to the mechanical properties (ductility, yield strength, and tensile strength) due to hydrogen for hydrogen charged MS-AHSS under fast loading that would simulate a crash situation.
4. The amount of hydrogen in the steels under the various testing conditions.

2.0 EXPERIMENTAL METHODS

2.1 Materials, solutions and LIST

Table 1 presents the chemical compositions and mechanical properties of the four commercial MS-AHSS: MS980, MS1180, MS1300, and MS1500, provided from commercial production. The mean sheet thicknesses were 1.2 mm for MS1300 and MS1500, 1.5 mm for MS980, and 1.8 mm for MS1180. The composition analysis was carried out by Spectrometer Services Pty Ltd, Coburg North, Vic. 3058, whilst the mechanical properties were supplied by the steel producer. The mechanical strength increased from MS980 to MS1500.

The microstructures of these steels were described previously [39]. The microstructure of all the steels was mainly martensite, with a grain size ~ 5 μm, with a ferrite content of 30%, 16%, 10% and 8% for MS980, MS1180, MS1300 and MS1500. The microstructure indicates that the steels were quenched from the inter-critical temperature, which transformed the austenite to martensite, and had no influence on the ferrite. The steels were provided as sheets from commercial production by the steel supplier, in the same condition as the steel is supplied to the auto industry for auto manufacture.

The three solutions were prepared using analytic grade chemicals and high grade

deionised water: (i) 3.5 wt% NaCl solution, (ii) 0.1 M HCl, and (iii) 0.1 M NaOH. These solutions were naturally aerated. Hydrogen charging was carried out at the free corrosion potential and at the zinc potential in the 3.5% NaCl solution to simulate extreme corrosion conditions for a car in service. The 0.1M HCl solution was used because this solution has been used by car manufactures [51,52]. Hydrogen charging was carried out in 0.1M NaOH because this solution was used in our prior study [39].

The linearly increasing stress tests (LIST) and fractography were carried out as in our prior research [39]. The threshold stress was determined using the potential drop method, as illustrated in Fig. 2.

The HE susceptibility index, *I*, was evaluated as follows [39]:

$$I = \frac{R_{\mathrm{A,air}} - R_{\mathrm{A,H}}}{R_{\mathrm{A,air}}} 100\% \quad (1)$$

where $R_{\mathrm{A,air}}$ is the reduction in area in air, and $R_{\mathrm{A,H}}$ is the reduction in area in the hydrogen charging environment. The HE index can range from 0% to 100%: (i) I = 0% indicates no HE susceptibility, whilst (ii) I =100% indicates high HE susceptibility due to the absence of plastic strain during fracture.

2.2 LIST in simulated service conditions

The four MS-AHSS was subjected to the LIST in 3.5 wt% NaCl to simulate corrosion in auto service. The specimen was placed in the charging cell, and affixed to the LIST apparatus. The charging cell was filled with 3.5 wt% NaCl solution, and the specimen was pre-charged for 24 h at 20 % yield stress with hydrogen under two charging conditions: (i) corrosion at the free corrosion potential, E_{corr}, and (ii) at the zinc potential, E_{Zn}, equal to -950 $\mathrm{mV_{Ag/AgCl}}$ (-752 $\mathrm{mV_{SHE}}$) (using a Pt counter electrode), to simulate service corrosion of galvanized steel with some steel free of the galvanising. LISTs were carried out under these conditions with stress rates corresponding to the 30 and 3 rph LIST motors. The small stress during pre-charging was applied so that the experiment was ready to run at the end of the pre-charging period without need of any further action on the specimen. A LIST was also conducted using MS1500 in 3.5wt% NaCl at the zinc potential, E_{Zn} (-752 $\mathrm{mV_{SHE}}$) at the slowest applied stress rate (0.0080 MPa $\mathrm{s^{-1}}$) and with a graphite (C) counter electrode, due to the concern regarding the use of a Pt counter electrode in 3.5 wt% NaCl, see Appendix A.

A corroding steel surface partly covered by zinc galvanising has a mixed potential that is between the free corrosion potential of the steel and the free corrosion potential of zinc. The fugacity of the hydrogen liberated at the steel surface increases with a more negative applied potential. The maximum amount of hydrogen that could be absorbed by a steel partly covered by zinc is therefore that which would be absorbed by the steel polarised to the free corrosion potential of zinc. Thus, the potential of freely corroded zinc was measured, and this potential was used as described above for pre-charging in the 3.5 wt% NaCl solution.

2.3 LIST in 0.1M HCl

LISTs of MS980 and MS1500 were also carried out in 0.1M HCl. The 0.1M HCl solution cannot be considered to be a typical service environment for an automobile. In fact, 0.1M HCl must be considered much more extreme than any environment likely to be encountered in normal automobile service. Nevertheless, tests in 0.1M HCl were included in this study because U-bend immersion test in 0.1M HCl have been used by car manufacturers to assess hydrogen delayed failures in automotive components [51,52]. MS980 and MS1500 have the least and the highest HE susceptibility of the four MS-AHSS [39]. Each LIST specimen was placed in the charging cell together with 0.1M HCl solution, and pre-charged for 24 h at 25% yield stress at the free corrosion potential. The LIST was carried at the free corrosion potential at a stress rate corresponding to the 3 rph motor. Two types of tests were conducted. The first test type used a bare LIST specimen, which was subjected to uniform corrosion. The second test type simulated crevice corrosion. A portion of the reduced cross-section area of the LIST specimen was covered with teflon tape prior to immersion in the acid solution. Crevice corrosion occurred at the boundary of the covered and uncovered sections.

2.4 Mechanical tests at substantial stress rates

Only MS1300 and MS1500 were tested because these were the most sensitive to hydrogen [39]. Each specimen was (i) fixed into the charging cell, (ii) attached to the LIST apparatus, (iii) pre-charged at an applied potential of -1700 $mV_{Hg/HgO}$ (-1602 mV_{SHE}) in the 0.1 M NaOH (pH 12.6) solution for 24 h with an applied stress of 20% of yield stress, (v) removed from the charging cell, and dried, and (v) tested using: (a) the LIST apparatus at the stress rates corresponding to the 30 and 300 rph motors, and (b) a conventional universal testing machine (UTM).

For testing in the LIST apparatus or the UTM, the specimen was removed from the charging solution, blow dried, mounted into the LIST apparatus or the UTM, and the LIST or UTM was started. The time between end of charging and start of test was less than 10 min to minimize hydrogen outgassing. Thus, the time-after-charge, prior to testing the specimen, was 10 min, and 24 h, and this information is included in the relevant specimen designation

The tensile tests conformed to the ASTM E 8 standard using the 5584 Instron universal testing machine (UTM) at a deformation rate of 0.015 mm/mm/min. This deformation rate was equivalent to 50 MPa s^{-1} in the initial elastic part of the test, which was about sixty times faster than the stress rate of 0.80 MPa s^{-1} using the 300 rph LIST motor.

2.5 Diffusible hydrogen concentration

Specimens were machined from the MS-AHSS sheets to a size of 10 mm x 50 mm x sheet thickness, using a water jet cutter. The specimens were mechanically ground on both sides to #1200 grit, rinsed with ethanol, and blow dried.

A three-electrode arrangement was used for electrochemical hydrogen charging of the specimens. The steel was the working electrode, a standard calomel electrode (SCE) was the reference electrode, and graphite was the counter electrode. The specimens were subjected to the following hydrogen charging conditions for 24 h: (i) corrosion at the free corrosion potential (E_{corr}) and at the zinc potential (E_{Zn}, -752 mV_{SHE}) in 3.5 wt% NaCl; (ii) corrosion at E_{corr} in 0.1 M HCl, and (iii) cathodic charging at -1848 mV_{SCE} (-1602 mV_{SHE}), -1548 mV_{SCE} (-1302 mV_{SHE}) and -1248 mV_{SCE} (-1002 mV_{SHE}) in 0.1 M NaOH. After hydrogen charging the specimens were removed from the solution, rinsed in deionized water, rinsed in ethanol, blow dried, and placed in the Bruker hydrogen analyser. The time from the end of hydrogen charging to specimen loading into the hydrogen analyser, was 3 min to minimize hydrogen outgassing in the specimens.

The diffusible hydrogen content was measured using the Bruker hydrogen analyser (G4 Phoenix GH), which uses the carrier gas hot extraction method and a thermal conductivity detector (TCD). Before the tests, the machine was calibrated following the standard procedures set by equipment manufacturer. Isothermal hydrogen desorption was performed at 400 ^{o}C. The amount of diffusible hydrogen in the specimen was obtained using the pre-installed analytical software.

2.6 Hydrogen permeation

2.6.1 Permeation procedure

Hydrogen permeation studies were conducted using a Devanathan-Stachurski type dual-cell electrolytic permeation arrangement [53], using the same approach as in our previous research [54]. Each compartment had the three-electrode system consisting of the working electrode (the steel specimen), the counter electrode (Pt), and the reference electrode (Hg/HgO in saturated 20% KOH). During the experiment, nitrogen was bubbled through the solution to remove the oxygen in the electrolyte.

Permeation specimens were machined from the MS sheet to have dimensions of 30 mm x 30 mm x sheet thickness, and ground on both sides with 1200 grit SiC. The exit side of the specimen was coated with palladium (Pd) to facilitate hydrogen oxidation and reduce signal noise. Oil and grease was removed from the specimen by soaking for 15 min in a degreasing solution (16 g NaOH,15 g Na_2CO_3, 15 g $Na_3PO_4.12H_2O$ and 2 mL liquid detergent dissolved in 500 mL distilled water) followed by a distilled water rinse. The specimen was immersed in a pickling solution of 37% HCl solution for 5 s to remove native surface oxide. The backside of the specimen was protected from the acid using adhesive tape. After pickling, the specimen was mounted in the plating cell. Palladium plating was carried in a 25% ammonia solution containing $PdCl_2$ at a concentration of 5 g L^{-1} for 5 min at a current density of 3 mA cm^{-2}. After Pd plating, the sample was rinsed with ethanol, air dried, and weighed to determine the thickness of the Pd layer. The Pd coating thickness was typically less than 1 μm.

The specimen was mounted in the permeation apparatus. The area of the specimen exposed to the solution was about 350 mm^2. The exit side, which had the Pd-coating, was polarized in the 0.1 M NaOH at an anodic potential of 300 $mV_{Hg/HgO}$. The anodic current at the exit cell was monitored using the PARSTAT 2273 potentiostat. After the background current at the exit cell reached 0.3 uA, the entry side of the specimen was cathodically charged at -1700 $mV_{Hg/HgO}$ (-1602 mV_{SHE}) in 0.1 M NaOH.

A pre-charging time of about 4 to 6 days, depending on the thickness of the specimen, was necessary to obtain a steady permeation current density, as in our prior studies [54,55]. Once the steady current was reached, successive partial decay (from -1700 to -1600, -1600 to -1400, and -1400 to -1100 $mV_{Hg/HgO}$) and build-up (from -1100 to -1400, -1400 to -1600, and -1600 to -1700 $mV_{Hg/HgO}$) transients were measured, as in our prior studies [54].

2.6.2 Data analysis

Prior research has shown that partial build-up or decay transients on a pre-charged steel membrane are associated with diffusible hydrogen that is free of surface effects [54,56]. The permeation rate, i_p, during a build-up or decay transient at time, t, can be expressed by [56]:

Build-up: $$\frac{i_p - i_p^0}{i_p^\infty - i_p} = \frac{2L}{\sqrt{\pi D_{eff} t}} \sum_{n=0}^{\infty} \exp\left(-\frac{(2n+1)^2 L^2}{4 D_{eff} t}\right) \quad (2)$$

Rise: $$\frac{i_p - i_p^0}{i_p^\infty - i_p^0} = 1 - \frac{2L}{\sqrt{\pi D_{eff} t}} \sum_{n=0}^{\infty} \exp\left(-\frac{(2n+1)^2 L^2}{4 D_{eff} t}\right) \quad (3)$$

where D_{eff} is the effective diffusion coefficient, L is the specimen thickness, i_p^0 is the initial permeation current density, and i_p^∞ is the steady-state permeation current density at that applied potential.

Mathematical modelling using MATLAB was used to fit the above permeation equations to the experimental transients to determine D_{eff}.

The concentration of hydrogen, C_H, at the entry side of the steel during charging in the permeation experiment is given by [54,56]:

$$C_H = \frac{i_\infty L}{F D_{eff}} \quad (4)$$

where i_∞ is the steady state permeation current density, L is the steel membrane thickness, and F is the Faraday constant (96485 C mol^{-1}).

3.0 RESULTS

3.1 LIST in 3.5wt% NaCl Solution

Table 2 presents values of the threshold or yield stress, σ_{TH}, the fracture stress, σ_F and the reduction in area, R_A, of the four MS-AHSS for LIST in air and in 3.5 wt% NaCl. There were slightly different applied stress rates for the different steels because of the differences in specimen thickness, which was related to the thickness of the steel sheets supplied. An applied stress rate of 0.8 MPa s^{-1} corresponded to a pre-yielding strain rate of 3.9 x 10^{-6} s^{-1}, whereas an applied stress rate of 0.0054 MPa s^{-1} corresponded to a pre-yielding strain rate of 2.6 x 10^{-8} s^{-1}. All the tests at at the zinc potential, E_{Zn}, were carried out with a platinum (Pt)

counter electrode, except for MS1500-Ezn-3-C, for which a carbon (graphite) counter electrode was used.

In air, the LIST measured the yield stress, σ_Y. For all steels, the mechanical properties were as expected, and were comparable with those provided by the steel supplier and to those values measured in our prior work [39]. There was ductile, cup and cone fracture.

In the 3.5wt% NaCl solution, the LIST can measure (i) the threshold stress, σ_{TH}, which is the stress at which sub-critical cracking starts in the specimen, or (ii) the yield stress, σ_Y, when subcritical cracking does not occur. For convenience, σ_{TH} was used for the LIST data (with the realisation that the measured quantity can be the yield stress), whilst σ_Y was used for UTM data (for which the measured quantity was the yield stress). It is stressed that, the use of σ_{TH} does not necessarily indicate the occurrence of subcritical cracking in the specimen. In this paper, the measured σ_{TH} was the yield stress.

Table 2 indicates that MS980 and MS1180 showed similar trends in their LIST results. At all applied stress rates (i.e. 0.064 and 0.0064 MPa s^{-1} for MS980, and 0.054 and 0.0054 MPa s^{-1} for MS1180) the σ_{TH}, σ_F, and R_A values of both steels were similar to those of their uncharged counterparts in air. This occurred for the two charging conditions, E_{corr} and E_{Zn}. All tests had an I value of zero, because of the minimal change in ductility of the specimens for these test conditions.

MS1300, tested at 0.080 MPa s^{-1}, displayed a slight reduction in σ_{TH} and σ_F for tests in the 3.5wt% NaCl solution, although R_A was unchanged. A somewhat greater reduction in σ_{TH} and σ_F occurred at the lower stress rate of 0.0080 MPa s^{-1}. The R_A had a slight decrease, and there was a corresponding increase of the value of I to 3. Furthermore, for both stress rates, the LIST values measured at E_{corr} and E_{Zn} were essentially the same.

For MS1500 tested at 0.080 MPa s^{-1}, σ_{TH}, σ_F, and R_A decreased slightly in the tests in the 3.5wt% NaCl solution, and there was negligible difference between the LIST values at E_{corr} and at E_{Zn}. At the lower rate of 0.0080 MPa s^{-1}, σ_{TH}, σ_F, and R_A were reduced somewhat further. Also the values obtained at E_{Zn} were slightly lower than those at E_{corr}, particularly for R_A. The specimen tested at E_{corr}, MS1500-Eo-3, had an I value equal to 3, whilst the specimen tested at E_{Zn}, MS1500-Ezn-3, has the highest value of I, which was equal to 10.

The percent decrease in σ_{TH} of the four steels ranged from 3-6%; whilst the decrease of σ_F ranged from 4-7%. The percent decrease in R_A was reflected by the HE index, *I*. Most *I* values were not significantly different from zero, ranging from 0 to 3. MS1500-Ezn-3 gave the highest *I* value of 10; however this value may still be regarded as small with respect to HE susceptibility.

The facture surfaces of all four MS-AHSS displayed a ductile cup-cone fracture, at all applied stress rates and charging conditions in the NaCl solution, expect for specimen MS1500-Ezn-3. Fig. 3 shows SEM images of a typical specimen after fracture. There was a clear neck. There were no surface cracks in the neck region, and also no cracks away from the neck region. Fig. 4 shows a typical fracture surface. The fracture surfaces showed the typical regions commonly associated with cup-cone fracture: the (i) central and the (ii) shear lip region. The central region contained microvoid coalescence (MVC) dimples, whilst the periphery consisted of MVC shear dimples. Typically, the dimples at the centre were rounder, larger and deeper than the shear dimples, indicating extensive ductility caused by tensile loading during the early stages of fracture. Shear dimples were parabolic, small and shallow due to the concentrated shear stress in the lip region, during the late stage of the fracture.

The size and depth of MVC dimples indicates the ductility of steel. Ductile metals possess large and deep dimples; conversely, a brittle metal has small and shallow dimples. With regard to these characteristics of MVC dimples, there was no discernible difference between the uncharged and hydrogen charged specimens for all the four MS-AHSS.

All specimens showed cup-cone fractures. Only MS1500-Ezn-3 showed an additional feature on the fracture surface, as illustrated in Fig. 5(a). There was a large secondary crack oriented parallel to the broad transverse side, that is parallel to the rolled surface of the steel sheet. The crack was deep and extended considerably from the centre to the short transverse side, as is evident from Fig. 5b. The crack originated from the centre, where the crack gap was widest, and propagated to the sides. MVC dimples were present in the central region, and there were no signs of brittle behaviour. It was difficult to determine if the crack propagation was intergranular or transgranular. There was crack propagation along the boundary of MVC dimples, which often coincided with a grain boundary, thus indicating the fracture to be at least partly intergranular and probably along prior austenite grain (PAG) boundaries.

The last entry in Table 2 presents the result of the LIST carried out using MS1500 at E_{Zn} (-752 mV_{SHE}) in 3.5% NaCl and with a graphite (C) counter electrode. There was (i) no change in the value of σ_{TH}, (ii) a small decrease in the value of σ_F, and (iii) a significant decrease in R_A, and consequently an increase in I. Fig 5d-f presents the facture surface. The fracture was shear with some necking. Cracking initiated at an edge and propagated diagonally. There were some brittle intergranular fracture features at the specimen edges, indicating an influence of hydrogen. The majority of the area consisted of MVC ductile fracture.

3.2 LIST in 0.1M HCl

Table 3 presents the LIST results for the MS-AHSS in 0.1M HCl at the free corrosion potential, at applied stress rates of 0.0064 and 0.0080 MPa s^{-1} for MS980 and MS1500, respectively, with uniform corrosion conditions (UC, specimens with "UC" in the specimen designation), and crevice corrosion conditions (CC, specimens with "C" in the specimen designation).

For MS980 and MS1500 with the uniform corrosion conditions, σ_{TH} and σ_F were slightly lower than the values in air. MS980 had an average reduction in σ_F of about 13%, whilst the reduction for MS1500 was 5%. There was a significant decrease in reduction of area (R_A). The mean I value was 50 and 85 for MS980 and MS1500, respectively.

For MS980 and MS1500 with crevice corrosion conditions, σ_F and R_A were significantly lower than their counterparts for tests in air. The σ_F was reduced by 50% and R_A had a low value of 8%. Both steels had similar I values of 89 and 87. The value of σ_{TH} was not measurable since the potential drop curve did not possess the typical indicator of σ_{TH}. This is attributed to the steel breaking at stresses lower than the yield stress.

Comparing the LIST values for the two corrosion conditions, the creviced MS980 steels showed lower strength and lower ductility than the non-creviced counterparts. The creviced MS980 has a higher HE susceptibility with an I value of 87, whilst the non-creviced steel has an average I value of 50. For MS1500, the strength of the creviced specimen was significantly lower than the non-creviced specimen. However, there was no significant difference in the R_A and I values; the creviced steel had an I value of 87 and the non-creviced steel had an average I value of 86.

Fig. 6 presents the fracture surface of MS980 and MS1500 in the un-creviced (uniform corrosion) condition. The two nominally identical MS980 specimens showed two different types of fracture, (i) cup-cone and (ii) shear fracture. The cup-cone fracture was accompanied by a modest amount of necking. Unfortunately, the fine features of the cup-cone fracture could not be resolved because a layer of oxide covered the fracture surface (which was attributed to the fact that the specimen had been a considerable time in the LIST cell after the end of the LIST). The shear fracture of the second MS980 specimen was associated with a lower value of fracture stress, a smaller value of the reduction in area, and consequently a higher value of the embrittlement index, *I*. Both specimens of MS1500 had shear fractures, similar to those for the second MS980 specimen. These were associated with a lower value of fracture stress, a smaller value of the reduction in area, and consequently a higher value of the embrittlement index, *I*.

Fig. 7 shows a magnified view of a typical shear fracture. The surface comprised of a fracture nucleation region, region 'T', and a fracture propagation zone, region 'S'. The fracture nucleation zone consisted of a mixture of intergranular and quasi-cleavage fracture, as shown in Fig. 7b. The fracture propagation zone mainly possessed shear MVC dimples, as shown in Fig. 7c, which became finer progressively away from the crack nucleation zone. There was some yielding near the crack nucleation zone of MS980 and MS1500, as is evident from Fig. 6. Furthermore, these specimens showed some necking, therefore it can be deduced that there was no subcritical crack growth, and all the fracture occurred at the ultimate tensile stress when the specimen had become mechanically unstable, and was undergoing locally ductile fracture.

Fig. 8 shows the typical magnified specimen surface of the MS1500 specimen after exposure in 0.1M HCl in the LIST. There was a black powder or residue at the specimen surface after the test. The surface revealed rough, broken and jagged features. Surface cracks were also present in some areas.

Fig. 9 presents the fracture surface of MS980 and MS1500 in the crevice corrosion condition. The SEM images were normal to the fracture surface and from the transverse broad side. The transverse view revealed shear-type fracture in both steels. The top view indicated that the two steels had similar fracture features, as indicated at higher magnification in Fig. 10 for the creviced MS1500. The fracture surface consisted of two distinct regions. There was a region of crevice corrosion at the periphery, marked region 'C', and a region of

shear fracture in the central area, marked as region 'S' and marked with the black rectangular boundary. Region S had two fracture zones: (i) a fracture nucleation zone and (ii) a fracture propagation zone. The fracture nucleation zone, marked 'N', contained quasi-cleavage fracture as shown in Fig. 10b. The fracture propagation zone, region 'G', consisted mostly of shear dimples, as illustrated in Fig. 10c. Furthermore, there were secondary cracks in the crack nucleation region in the creviced MS1500, but not in MS980. The secondary crack illustrated in Fig. 10b had considerable length and propagated near the boundary of the creviced section. Like the secondary crack in Fig. 5, the secondary crack in Fig. 10 was also largely parallel to the rolled surface of the sheet, and probably has similar causes.

3.3 XPS analysis

One possible concern with a platinum counter electrode in a chloride-bearing solution (e.g. NaCl) is the possibility of platinum (Pt) dissolving at the counter electrode, plating out at the working electrode [57], and influening the hydrogen uptake of the steel. SEM and XPS analyses were conducted to determine if there was detectable Pt on specimen surfaces.

MS1180 charged at E_{Zn} in 3.5% NaCl was examined because MS1180 had the longest exposure (a total of 4 d) to cathodic hydrogen charging in the 3.5wt% NaCl solution during LIST. SEM analysis of the steel did not indicate the presence of any detectable platinum on the surface. Similarly, the XPS spectra, typical examples are given in Figs. 11 a and b, indicated that there was no detectable Pt on the surface of the MS1180. This implies that the use of a Pt counter electrode in these experiments did not cause a measureable amount of Pt on the surface, which could have influenced the hydrogen uptake of the steels in these 3.5 wt% NaCl solutions.

XPS analyses were also carried out of MS1180 cathodically charged in the 0.1 M NaOH using a Pt counter electrode at -1700 $mV_{Hg/HgO}$ (-1602 mV_{SHE}) at the fastest (300 rph, a total of 1 d pre-charging and 45 min test time) and the slowest (3 rph, a total time of 4 d) applied stress rates. In both specimens, Pt was detected at the surface, as illustrated in Fig. 11 c and d. This indicates that hydrogen ingress in the steel charged in the alkaline solutions may have been influenced by the presence of Pt.

XPS analyses were also carried out of MS1500 cathodically charged in the 0.1 M NaOH using a C counter electrode at -1700 $mV_{Hg/HgO}$ (-1602 mV_{SHE}) for 5 days. There was

some carbon on the surface attributed to the typical carbon contamination on the surface of XPS specimens. This surface carbon contamination was rapidly removed by etching with Ar ions, revealing a surface containing Fe, O and only a residual amount of C. The surface was clean with no detectable surface contamination.

Appendix A presents experiments carried out to study the influence of the counter electrodes on hydrogen content in MS-AHSS during cathodic charging in 0.1 M NaOH. Appendix A indicates that the Pt counter electrodes (i) decreased by ~ 70% the steady state H uptake of MS1500 during cathodic charging in 0.1 M NaOH (compared with the case of a carbon, C, counter electrode) and (ii) had little influence on hydrogen diffusion in the steel and hydrogen egress from the steel. There was nevertheless a substantial amount of hydrogen in the steel under these charging conditions. This means that Pt counter electrodes should be used with caution during hydrogen embrittlement studies involving cathodic hydrogen charging.

Similarly Fig. A1 and Table A1 indicate that MMO-Ti counter electrodes should be avoided in such studies.

3.4 Tests at substantial stress rates

Table 4 presents the LIST data for MS1300 and MS1500, tested (i) unchanged in air (tests designated uncharged/air), (ii) in air essentially immediately after hydrogen charging in 0.1M NaOH at an applied potential of -1700 $mV_{Hg/HgO}$ (-1602 mV_{SHE}) for 24 h at 20% yield stress (tests designated NaOH/Air, specimen designation includes 10 min), (iii) in air 24 h after hydrogen charging in 0.1M NaOH at an applied potential of -1700 $mV_{Hg/HgO}$ (-1602 mV_{SHE}) for 24 h at 20% yield stress (tests designated NaOH/Air, specimen designation includes 24H), and (iv) in 0.1M NaOH at an applied potential of -1700 $mV_{Hg/HgO}$ (-1602 mV_{SHE}), after hydrogen charging in 0.1M NaOH at an applied potential of -1700 $mV_{Hg/HgO}$ (-1602 mV_{SHE}) for 24 h at 20% yield stress (tests designated NaOH/NaOH). All the hydrogen charging involved a Pt counter electrode. The purpose of these experiments was to understand the influence on the hydrogen on MS-AHSS of (i) fast stress rates, and (ii) holding times after charging. Initial results indicated that there was no hydrogen sensitivity at 10 min, so that tests at longer holding times would be expected yield results similar to those in the 10 min test. Indeed, the tests at 24 h confirmed this hypothesis, as is clear from Table 4

from specimens MS1300-24H-300, MS1300-24H-30, and MS1300-24H-UTM. Consequently, tests at longer times were not carried out.

Table 4 indicated that the mechanical properties of the uncharged steels measured using the LIST and the conventional tensile test using the UTM were similar. This is clear from a comparison of specimens MS1300-A-UTM and MS1300-A-UTM. This indicates that the LIST apparatus was correctly calibrated, and was capable of carrying out accurate measurements of the mechanical properties of these steels.

Table 4 further indicates that, for the hydrogen charged specimens tested in air (S/Air), for both MS1300 and MS1500, there was no significant HE susceptibility in the steels at all the stress rates tested. The two steels followed similar trends. The hydrogen-charged steels subjected to LIST at 0.080 and 0.0080 MPa s^{-1} gave values of σ_{TH}, σ_F and R_A similar to their uncharged counterparts. The hydrogen-charged specimens gave a slightly lower σ_Y, σ_F and R_A in the UTM test compared to similarly tested uncharged steels. The highest I values of 4 and 8 were for the hydrogen-charged steels MS1300 and MS1500 subjected to tensile testing (MS1300-10min-UTM and MS1500-10min-UTM). This indicates that only the hydrogen-charged specimens tested with the UTM showed any indication of a hydrogen effect, although this effect may be considered not to be significant.

The fracture mode in all the specimens was ductile cup-cone fracture accompanied by considerable necking. Fig. 12 presents an example of the typical fracture of the steels. There were the typical fracture zones, i.e. the central and shear lip region, associated with cup-cone fracture. There were round and parabolic MVC dimples in the central and the shear lip regions, respectively. There were some small secondary cracks parallel to the rolled surface.

A detailed examination of the fracture surfaces of two specimens; namely, MS1300-10min-UTM and MS1500-10min-UTM, revealed some degree of reduced ductility in these steels. Fig. 13 and Fig. 14 present the MVC shear dimples in the shear lip region of the uncharged and hydrogen-charged MS1300 and MS1500 steels, respectively. These images show that the hydrogen-charged specimen had smaller and shallower dimples, whilst the uncharged steel had larger, deeper and more elongated parabolic shear dimples. This indicates that hydrogen had some influence of the ductile microvoid coalesce fracture process.

Table 4 also includes results of LIST with simultaneous in situ hydrogen charging of MS1300 and MS1500. The tests were carried out in 0.1 M NaOH at a charging potential of -1700 $mV_{Hg/HgO}$ (-1602 mV_{SHE}) and at two different stress rates of 0.80 and 0.080 MPa s^{-1}. These were the specimens: MS1300-H1.7-30, MS1500-H1.7-30, MS1300-H1.7-300 and MS1500-H1.7-300.

At an applied stress rate of 0.80 MPa s^{-1}, there was no appreciable difference in the σ_{TH}, σ_F and R_A of the hydrogen charged steels compared to their uncharged counterparts. The fracture mode was cup-cone accompanied by extensive necking, as shown in Fig. 15a. At the lower stress rate of 0.080 MPa s^{-1}, there was a small reduction in σ_{TH} and σ_F, and a substantial reduction in R_A. The decreased ductility caused the high values of I; i.e. 50 and 89 for MS1300 and MS1500, respectively. The fracture mode also changed from cup-cone to macroscopically brittle shear fracture, as shown in Fig. 15b. These results confirmed the results of our previous research on MS-AHSS [40], which indicated considerable HE susceptibility in the two steels at low stress rates and with hydrogen charging concurrent with mechanical stressing.

3.5 Diffusible hydrogen concentration

Table 5 presents the measured diffusible hydrogen concentration, C_{DH}, in the three MS-AHSS: MS980, MS1300 and MS1500. The type of hydrogen measured at the desorption temperature of 400 ^oC is considered diffusible hydrogen, which includes weakly trapped hydrogen [58].

Fig. 16 presents the measured diffusible hydrogen concentration as a function of the applied overpotential, η, which was evaluated using [55]:

$$\eta = E_c - E_H^0 \quad (5)$$

where E_c is the applied potential, and E_H^0 is the equilibrium potential for hydrogen in the charging solution. E_H^0 was calculated using the Nernst equation as [59]:

$$E_H^0 = -0.0591pH - 0.0295\log f_{H_2} \quad (6)$$

where f_{H_2} is the hydrogen fugacity, which in this case was equal to unity. The use of η, instead of the applied potential, provides an appropriate basis for comparing the results for the different solutions.

All the as-received specimens possessed negligible amounts of hydrogen, with a mean diffusible hydrogen concentration of 0.003 μg g^{-1}.

The diffusible hydrogen concentrations were higher in the steels immersed in 3.5 wt% NaCl at the open circuit potential, E_{corr}, and were higher still in the steels immersed in 3.5% NaCl and polarised at the zinc potential, E_{Zn} (-752 mV_{SHE}).

The highest values of the diffusible hydrogen concentration, C_{DH}, were in the steels that were cathodically charged in 0.1M NaOH solution. The diffusible hydrogen content was expected to increase with increasingly negative overpotential. Indeed, the measured diffusible hydrogen concentration increased between hydrogen charging at -1248 mV_{SCE} (-1002 mV_{SHE}) and -1848 mV_{SCE} (-1602 mV_{SHE}). However, there was the highest hydrogen concentration for hydrogen charging at -1548 mV_{SCE} (-1302 mV_{SHE}) in all three steels.

The diffusible hydrogen concentration of MS-AHSS immersed in 0.1 M HCl at E_{corr} had values in between those immersed in 3.5% NaCl and cathodically hydrogen charged in 0.1 M NaOH, and approached the diffusible hydrogen concentrations in 0.1 M NaOH at -1248 mV_{SCE} (-1002 mV_{SHE}).

3.6 Hydrogen permeation

Table 6 presents the measured values of the effective hydrogen coefficient, D_{eff}, and the total hydrogen concentration on the input side of the specimen, C_H, for MS980, MS1300 and MS1500 measured from the hydrogen permeation transients. Fig.17 shows a typical decay and rise permeation transient loop that was used for analysis. D_{eff} was calculated in each case by fitting the appropriate permeation equation (Eq.s 2 or 3) to the experimental data, as shown in Fig. 18a and 18b.

The values of the hydrogen diffusion coefficient, D_{eff}, for the three steels ranged from 10.2 to 11.3 x 10^{-7} cm^2 s^{-1}. MS1300 had the highest values of the hydrogen diffusion coefficient, followed by MS980, then MS1500. However, the differences between the

measured D_{eff} among the three steels was small. The D_{eff} values increased with a more negative hydrogen charging potential consistent with our prior research [54].

Table 6 indicated that MS1300 had the highest hydrogen concentration after cathodic hydrogen charging, whilst MS980 and MS1500 had almost similar hydrogen concentrations. This observation agrees with the diffusible hydrogen measurements, where MS1300 showed the highest hydrogen content, and MS1500 and MS980 had similar concentrations.

4.0 DISCUSSION

4.1 As-received steels

The steels MS980, MS1180, MS1300 and MS1500 were from normal commercial production. Thus it must be assumed that these steels were representative, including containing an amount of hydrogen representative of their production. Table 2 indicates that, in all cases, the mechanical properties were as expected. The fractures were in all cases associated with significant necking and ductility. This indicates that there was minimal influence of hydrogen for the steels in the as-received condition. This is consistent with the fact that there was essentially no diffusible hydrogen in the steels under these conditions, as is clear from Fig. 16.

4.2 Tests in 3.5 wt% NaCl

4.2.1 Pt counter electrode

It is expected that corrosion of the steel causes the evolution of some hydrogen by the associated cathodic partial reaction. For corrosion in a neutral solution, the main cathodic partial reaction is expected to be the oxygen reduction reaction, although it is expected that some of the cathodic partial reaction is hydrogen evolution, which is relatively slow in neutral solutions because of the low concentration of H^+ ions.

The tests in 3.5 wt% NaCl are considered to represent an extreme of the corrosion conditions to which these steels may be expected to be exposed to during auto service. High salt contents can occur in marine exposures, and due to de-icing salts in cold (snowy) climates. More often the automobiles will be subjected to much milder conditions, such as

rain (causing corrosion in a dilute neutral solution), atmospheric corrosion, or dry conditions in a garage. Consequently, it is important to understand the influence of hydrogen on these steels in these most-severe of the possible corrosion conditions to which the automobile is exposed to in service.

The tests in 3.5 wt% NaCl at E_{corr} represent the corrosion situation where bare steel sheet is immersed in the saltwater, whilst those at E_{Zn} simulate the case of a bare steel surface exposed to a galvanized surface in a similar environment. The measured E_{corr} was -350 $mV_{Ag/AgCl}$ (-152 mV_{SHE}) whilst E_{Zn} was -950 $mV_{Ag/AgCl}$ (-752 mV_{SHE}). Due to a more cathodic potential, it is expected that more hydrogen was produced at E_{Zn}. Indeed, hydrogen evolution at an actual Zn coating has been reported [60]. This means that the possibility for HE at E_{Zn} is higher than at E_{corr}.

Table 2 did indicate a slight reduction in σ_{TH}, σ_F and R_A, in all cases including those at E_{Zn} with a Pt counter electrode. These results indicate that the influence of hydrogen was small for the four MS-AHSS in the 3.5 wt% NaCl solution at all charging potentials and applied stress rates. This is consistent with the zero or low I values, and the occurrence of ductile cup-cone fracture in all specimens. Only MS1500-Ezn-3 showed some indications of an influence of hydrogen. These indications included (i) the small reduction in R_A, and (ii) the secondary cracks in the central region of the fracture face. These secondary cracks are attributed to have formed in the late stages of fracture. The mechanism of cup-cone fracture involves crack nucleation at the centre of the specimen coincident with intense plastic deformation. The ductile crack grows and propagates from the core towards the surface. At the last stage of fracture, there are significant tensile stresses normal to the principal applied stress just before final separation of the mating pieces, and the ductile secondary cracks are attributed to the action of these stresses.

Hydrogen can cause macroscopically brittle failure by enhancing dislocation motion and causing localized plastic deformation, as postulated in the hydrogen-enhanced local plasticity (HELP) mechanism [61,62]. Fig 5 indicated that the secondary crack originated at the central region of the fracture surface. The plane of this ductile fracture is consistent with the expected fibre structure of the steel sheet due to the working operations. Thus, the ductile cracking is attributed to an interaction of hydrogen with a slight metallurgical heterogeneity at the final stages of the ductile fracture. The secondary cracking occurred amid intense ductile plastic deformation as indicated by the presence of MVC dimples on the fracture

surface, and the significant necking indicated that the specimen was mechanically unstable and was undergoing ductile fracture.

It is worth noting that the only measureable influence of hydrogen was this ductile secondary cracking only for MS1500 tested at the lowest applied stress rate of 0.0080 MPa s^{-1} in the 3.5 wt% NaCl solution, and only at E_{Zn}. Even under these most severe of the simulated service conditions, there was only a slight influence of hydrogen, and only during the final fracture, when the specimen was mechanically unstable and was undergoing ductile fracture.

It is also worth noting that there was no indication of any subcritical crack growth associated with hydrogen.

High strength steels can suffer delayed fracture in NaCl solution associated with hydrogen [32]. Furthermore, a critical amount of hydrogen is necessary to cause embrittlement. It can be thus concluded that the absence of an influence of hydrogen on the four MS-AHSS in 3.5 wt% NaCl solution can be attributed in part to the low amount of hydrogen produced in this environment. This is confirmed by the low diffusible hydrogen content measured in the steels after charging at these conditions, as shown in Fig. 16. E_{corr} was equivalent to -350 $mV_{Ag/AgCl}$ (-152 mV_{SHE}), whilst E_{Zn} was -950 $mV_{Ag/AgCl}$ (-752 mV_{SHE}). Clearly, corrosion at these potentials is inadequate to produce hydrogen at concentrations that exceed the critical concentration. Conder et al [63] reported similar observations whilst investigating HE susceptibility of low carbon martensite (LCMS) steels, a material similar to MS-AHSS. The LCMS did not show significant HE susceptibility in NaCl solutions even at high-applied cathodic potentials in the range of -700 to -1300 mV_{SCE} (-454 to -1054 mV_{SHE}). They proposed that the absence of an influence of hydrogen was due to the low levels of hydrogen produced in these solutions. At -900 mV_{SCE} (-654 mV_{SHE}), they measured only 0.2 ppm hydrogen in the steel after 1 day of charging; whilst at the highest applied potential of -1300 mV_{SCE}(-1054 mV_{SHE}), the hydrogen content was only 1.3 ppm. In the current study the highest charging potential was -950 $mV_{Ag/AgCl}$ (-752 mV_{SHE}), which is equivalent to -998 mV_{SCE} (-752 mV_{SHE}). Using the data from Conder et al and assuming comparable hydrogen uptakes between the two steels, this means that the hydrogen content in the MS-AHSS would only be slightly higher than 0.2 ppm at the applied potential of -950 $mV_{Ag/AgCl}$ (-752 mV_{SHE}). This is consistent with the expectation that the steels, in the current study, were exposed to only small amounts of hydrogen. Conder et al even added hydrogen recombination poisons in the salt solution, in an attempt to enhance hydrogen uptake in the steels and induce a HE

response. However, in spite of the observed increase in hydrogen uptake, the LCM steels still did not show significant HE.

There was no discernible difference in the performance of the steels in 3.5wt% NaCl at E_{corr} and E_{Zn}, but this does not necessarily imply that a zinc coating is inconsequential for MS-AHSS in actual service. In fact, there were some signs of an influence of hydrogen in MS1500-Ezn-3, and this was attributed to the more negative applied potential. Similarly, Payer et al [64] concluded that a zinc coating can increase HE susceptibility of low carbon martensite steels, due to the relatively higher ease of hydrogen evolution at the lower potential of zinc. They also found that other metal coatings such as chromium offered better protection against HE.

4.2.2 Carbon counter electrode

The last entry in Table 2 presents the result of the LIST carried out using MS1500 at E_{Zn} (-752 mV_{SHE}) in 3.5% NaCl and with a graphite (C) counter electrode. There was (i) no change in the value of σ_{TH}, (ii) a small decrease in the value of σ_F, and (iii) a significant decrease in R_A, and consequently an increase in I. Fig 5d-f presents the facture surface. There was some necking, which indicated that the fracture also occurred at the ultimate tensile strength, when the specimen had become mechanically unstable. Intergranular cracking initiated at an edge and propagated diagonally. The majority of the area consisted of MVC ductile fracture.

These observations indicate that the influence of hydrogen was somewhat greater in the case of the experiment carried out using a carbon counter electrode, nevertheless, the influence of hydrogen occurred only at the ultimate tensile strength when the specimen had become mechanically unstable. There was then a contribution of hydrogen fracture events that contributed to the fracture, and decreased the overall ductility. It is also worth noting that there was no indication of any subcritical crack growth associated with hydrogen.

4.3 Time for hydrogen saturation

The value of the diffusion coefficient, D_{eff}, measured using the permeation experiments can be used to estimate the saturation time, i.e. time during charging at which the concentration at the inside of the specimen is equal to that of the surface. This estimate applies to the charging carried in the LIST.

Hydrogen diffusion is assumed to occur from both sides of a thin plate of thickness, L. The initial and boundary conditions for this diffusion case are as follows:

$C = 0$, $x = -L/2 = L/2$ (surface), $t = 0$; (7)

$C = C_o$, $x = -L/2 = L/2$ (surface), $t > 0$; $\frac{\partial C}{\partial x} = 0$, $x = 0$ (center), $t > 0$ (8)

where C is the hydrogen concentration, the initial uniform hydrogen concentration is zero at $t = 0$; the surface concentration becomes C_o at both surfaces for $t > 0$, and the diffusion at the centre of the plate is the same in both directions from the two surfaces, so that the concentration gradient at the plate centre remains zero for $t > 0$. For these conditions, the solution to Fick's second law is [65] :

$$\frac{C}{C_o} = 1 - \frac{4}{\pi}\sum_{n=0}^{\infty}\frac{(-1)^n}{2n+1}\exp\left\{\frac{-D_{eff}(2n+1)^2\pi^2 t}{4L^2}\right\}\cos\frac{(2n+1)\pi x}{2L} \quad (9)$$

Fig. 19 presents a plot of C/C_o vs time for MS980 and MS1500. The diffusion model indicates that less than 5 h of charging was needed to ensure that the concentration at the specimen center reached 99.9% of the surface concentration, and the specimen effectively reached hydrogen saturation. This implies that the 24 h charging period used in the current study ensured complete hydrogen saturation of the specimens.

4.4 Uniform corrosion in 0.1 M HCl

As stated previously, corrosion in 0.1M HCl is considered to be much more severe than the corrosion environments encountered in auto service. This environment was included in this study to allow a comparison with typical service, because some car manufacturers have been using 0.1M HCl to study the influence of hydrogen on auto steels, e.g. Horvath et al [52].

The unstated assumption in these experiments is that any decrease in strength and ductility is attributable to the hydrogen adsorbed by the steel due to the corrosion of the steel in the 0.1M HCl. It is assumed that there is no influence on the fracture processes of the significant corrosion rate of the steel. This assumption may not be correct, as there may be anodic stress corrosion cracking due to the substantial corrosion rate of the steel in the 0.1 M HCl, and this substantial corrosion could interact with the applied stress to cause stress corrosion cracking.

Table 3 shows that, under uniform corrosion conditions, MS980 showed an apparent influence of hydrogen, and MS1500 showed a greater apparent influence of hydrogen. This is indicated by (i) the *I* values of 42 and 57 for MS980 and 84 and 87 for MS1500 (Table 3), and (ii) the shear fractures as indicated in Fig. 6. Nevertheless, Fig. 6 indicates that both steels showed significant necking, which indicates that the apparent influence of hydrogen on both steels was to influence the final ductile fracture process, and there was no subcritical crack growth.

For comparison, Zhou et al [51] subjected MS980 to a U-bend immersion test in 0.1 M HCl, and found no significant HE, whereas the present LIST tests indicated an apparent influence of hydrogen. This difference in results may be attributed to the different modes of stressing done in each study. The current study used a dynamic applied stress, while the study by Zhou et al used a static applied load. This indicates that dynamic loading or stressing is more severe than static loading in the HCl solution, and can cause an apparent embrittlement response from MS980. In agreement were the observations by Zhou et al of apparent HE susceptibility of MS980 when subjected to the slow strain rate test (SSRT) in 0.1 M HCl. Their results were similar to those reported herein: in the presence of hydrogen, MS980 showed (i) some decrease of the yield stress, ultimate tensile stress, and elongation to fracture, and (ii) ductile fracture.

These results indicate that, in the presence of 0.1M HCl and slowly increasing loading, MS980 and MS1500 show a decrease of yield and tensile strength, a decrease of ductility, mainly ductile fracture, and no sub-critical crack growth.

Clearly, the 0.1M HCl environment was quite severe, and caused an apparent influence of hydrogen on MS980 and MS1500. This appears to be consistent with the literature. For example, Willan [66] noted that even a 30 second HCl pickling caused HE in 4340 high strength steels. They recommended the use of fast pickling times and low pickling acid concentration if the treatment to avoid HE. Otherwise, pickling should be avoided whenever possible, or the hydrogen outgassed by heating to ~200 ^{o}C.

MS1500 showed an apparent hydrogen sensitivity higher than that of MS980 in 0.1 M HCl. This could be attributed to the higher strength of MS1500, and the fact that hydrogen sensitivity increases with steel strength.

Fig. 16 indicates that the steels tested in in 0.1 M HCl had hydrogen concentrations slightly lower than those hydrogen cathodically charged in 0.1M NaOH at -1200 $mV_{Hg/HgO}$ (-1002 mV_{SHE}). Thus it is pertinent to compare the LIST results for MS980 and MS1500 whilst exposed to 0.1M HCl with the LIST results for MS980 and MS1500 whist subjected to hydrogen cathodic charging at -1200 $mV_{Ag/AgCl}$ (-1002 mV_{SHE}) in 0.1M NaOH from our previous study [39]. Table 3 shows that the hydrogen embrittlement index measured in the present work in 0.1M HCl was 42 and 57 for MS980 and 84 and 87 for MS1500. In comparison, in our prior work [39], the hydrogen embrittlement index, whilst subjected to hydrogen cathodic charging at -1200 $mV_{Ag/AgCl}$ (-1002 mV_{SHE}) in 0.1M NaOH was much lower at 3 for MS980, but was comparable for MS1500.

This comparison for MS980 indicates that in 0.1M HCl there are factors additional to the hydrogen content that reduce the ductility of the fractures in this solution.

4.5 Crevice corrosion in 0.1M HCl

Table 3 indicates that, under crevice corrosion conditions, the mechanical responses of MS980 and MS1500 were similar. The (engineering) fracture stress was decreased significantly, the reduction of area was also decreased significantly, so that the values of susceptibility index, I were 89 and 87. This indicates that the behaviour of the steels was independent of the mechanical strength and factors such as composition and microstructure. The strength and ductility were determined largely by the depth of the crevice, which was influenced by the rate of corrosion in the steels. As the crevice deepened, the load-bearing area decreased until fracture. Fracture occurred when the stress in the remaining ligament reached a critical stress, usually equal to the notched or constrained tensile strength of the steel. Therefore, the actual strength of the steel may be obtained by considering the remaining load-bearing area at fracture. This area was measured from the SEM images of the fracture surfaces, as presented in Fig. 9. The actual fracture strength of MS980 and MS1500 was equal to 1280 and 1720 MPa, respectively. The actual tensile strength values were slightly higher than the corresponding values in air, attributed to some notch strengthening and indicating that the steel was not significantly weakened in the acidic environment. The values of tensile strength in Table 3 were simply the result of considering the initial area when calculating the stress and not accounting for the effective area at fracture. The crevice also acted as a notch and caused the low R_A and high I values for the steels. The crevice caused

fracture prior to plastic deformation. Hence, there was minimal difference between the initial and final cross sectional area of the specimen that resulted in the low values of R_A. However, further interpretation of these results is not possible because there were no comparable notched tensile tests with uncharged specimens.

4.6 Tests at substantial stress rates

Table 4 indicated that there was no influence of hydrogen at substantial stress rates. The hydrogen charged MS1300 and MS1500 tested in air at substantial stress rates (i.e. ranging from 50 to 0.080 MPa s^{-1}) had values of yield strength, tensile strength and ductility equal to the corresponding values of the uncharged steels. In addition, Table 4 indicated that, for the LIST at 0.8 MPa s^{-1}, there was no influence of hydrogen on hydrogen charged MS1300 and MS1500 subjected to LIST whilst undergoing hydrogen charging. In contrast, Table 4 indicates that, there was an influence of hydrogen at slow applied stress rates of 0.08 MPa s^{-1}, for hydrogen charged MS1300 and MS1500 subjected to LIST whilst undergoing hydrogen charging, as illustrated by samples MS1300-H1.7-30 and MS1500-H1.7-30.

Two conclusions may be drawn from these observations.

Firstly, there is a critical stress rate above which there is no significant influence, even in the presence of hydrogen during stressing. In the current study, the critical stress rate was 0.8 MPa s^{-1} at a hydrogen fugacity equivalent to -1700 $mV_{Hg/HgO}$ (-1602 mV_{SHE}). Indeed, past studies have indicated that HE of steels occurs at low strain rates [67-69], low applied stress rates [12,39,47,48], or for static loading [70]. It is also expected that the value of the critical stress rate is influenced by factors such as hydrogen fugacity, strength of steel and microstructure.

Secondly, in situ hydrogen charging during the mechanical test can influence the HE behaviour of the steels, and that the lack of HE susceptibility in the MS-AHSS in the tests without concurrent hydrogen charging may have been due to (i) simply the lack of a hydrogen effect, or (ii) the combined effects of the high stress rates and hydrogen outgassing. Outgassing can reduce the overall hydrogen content to levels lower than the critical concentration necessary for embrittlement. Hydrogen can ingress and egress from metals with relative ease due to the small size of the hydrogen atom [60]. Hydrogen diffuses into the steel and saturates the lattice during charging. Conversely, hydrogen starts to egress the steel

as soon as hydrogen charging stops, unless hydrogen is strongly bound by traps. Zwettler et al [71] reported that the total amount of hydrogen escaping from AHSS at room temperature was exponential with time; thereby, highlighting the importance of minimizing transfer times between charging and the hydrogen testing. Oudriss et al [72] observed that most of the hydrogen adsorbed by a martensitic steel after electrochemical charging had completely diffused out after 3 days. Furthermore, Willan et al [66] noted the 'room temperature relief' of hydrogen-charged AISI 4340, in which there was a room temperature dwell time of at least 2 hours after acid contact, was enough to significantly lower HE in the steel. They attributed this relief to hydrogen outgassing.

Lee et al [73] measured the amount of hydrogen in press-hardened 22MnB5 immediately after charging, and after the tensile test. The tensile test was conducted at a crosshead speed of 2.54 mm/min. They found that (i) a hydrogen concentration of 1.7 ppm was enough to cause considerable HE in the steels, and (ii) the hydrogen concentration of the steels, regardless of microstructure, stayed constant within the test duration. In the current study, the crosshead speed in the tensile test was 0.5 mm/min, about 5 times slower than that used by Lee et al. and so more hydrogen may have been lost. On the other hand, a study by Oudriss et al [72] reported that the HE susceptibility of martensitic AISI 5135 was highest within the first 15 to 24 hours at room temperature after hydrogen charging. They proposed that hydrogen mobility in the steel was highest during this interval that resulted in the heightened HE response. However, the outgassing kinetics depend critically on the steel type and the associated density and distribution of hydrogen traps.

Lovicu et al [36] did somewhat similar tests and found significant hydrogen embrittlement, as measured by a decrease in the notched ultimate tensile strength, for a hydrogen concentration above 3.7 ppm for M1200 (similar to MS1300 used in the present study), and for a hydrogen concentration above 1 ppm for M1400 (similar to MS1500 used in the present study). They charged each notched MS-AHSS specimen electrochemically, carried out a slow strain rate test (SSRT) at a strain rate of 4.5×10^{-5} s^{-1}, and measured the amount of hydrogen in half of each tensile specimen after the SSRT compared with a witness specimen charged at the same time as the SSRT specimen. The duration of their SSRT can be estimated at ~1.3 min. Considering what is involved in mounting an SSRT specimen, and removing the SSRT specimen at the end of the SSRT and taking the specimen to the hydrogen content analyser, it is likely that the total time was at least ~10 min between the end of the electrolytic charging and the start of the hydrogen content analysis. They found that the

hydrogen content after the SSRT was within 10% of that of their witness samples, indicating that there was little hydrogen lost from the sample in this period of time. This time was comparable to that taken in this study between the end of the cathodic hydrogen charging and the UTM tests. This indicates that the UTM tests in the current research would have observed hydrogen embrittlement in the MS1300 and MS1500 specimens if there was hydrogen embrittlement. The lack of hydrogen embrittlement in the UTM tests of hydrogen charged MS1300 and MS1500 is thus attributable to there being no hydrogen embrittlement of MS1300 and MS1500 under the conditions tested. The current study did not use recombination poisons, and thus the hydrogen content is expected to be lower.

The amount of hydrogen remaining in the steels in the present LIST experiments of Table 4 as a function of time after hydrogen charging may be estimated using the appropriate diffusion model. For a diffusion model of a thin plate with thickness, L, with a uniform initial hydrogen concentration of C_o, with hydrogen outgassing occurring at both sides; there are the following initial and boundary conditions:

$C = C_o$, $0 < x < L$, $t = 0$ (10)

$C = 0$, $x = 0$, L (surface), $t > 0$ (11)

And the solution to Fick's second law is [74]:

$$\frac{C}{C_o} = \frac{4}{\pi}\sum_{n=0}^{\infty}\frac{1}{2n+1}\sin\left[(2n+1)\pi\frac{x}{L}\right]\exp\left[-\frac{(2n+1)^2L^2Dt}{L^2}\right] \quad (12)$$

This equation provides the value of the normalised concentration, C/C_o after any elapsed time, t, which when integrated yields the amount of hydrogen remaining in the steel. Fig. 20 plots the fraction of hydrogen remaining in MS980 and MS1500 for specimens of thicknesses as used in these tests.

The high stress rate in the tensile tests ensured a rapid test, estimated to be about 3 minutes per tensile test compared to 30 min and 4 h needed for the LIST tests at 0.8 and 0.08 MPa s^{-1}. The hydrogen outgassing model (Eqn. 12) indicates that about 85% of the charged hydrogen remains after 8 min (total time of standard tensile test and processing time after charging), 75% after 30 min, and about 30% after 4 hours. This indicates that, except for the LIST at the slowest stress rate of 0.008 MPa s^{-1}, the steels possessed substantial amounts of hydrogen during the tensile tests and the LIST tests.

This means that the UTM tests of hydrogen charged MS1300 and MS1500 do indeed indicate the absence of any macroscopic influence of hydrogen on the yield strength, fracture strength, and ductility.

This is reinforced by a lack of a significant hydrogen effect for the pre-charged specimens subjected to LIST whilst being subjected to hydrogen charging, see MS1300-H1.7-300 and MS1500-H1.7-300 in Table 4.

Figs. 13 and 14 do however indicate that the presence of hydrogen did have some influence on the details of the microscopic fracture process as the hydrogen charged specimens had smaller shallower dimples on the fracture surface. This is consistent with the hydrogen enhanced plasticity model, and consistent with hydrogen enhancing microscopic plastic flow.

The considerations about hydrogen egress also indicate that any influence of hydrogen may be fairly rapidly dissipated once the hydrogen source (corrosion) becomes inactive.

4.7 Metallurgical influences

The fractography in Figs. 5, 10 and 12 indicate that under some conditions there were secondary cracks parallel to the rolled surface of the steel sheet. These ductile secondary fractures are consistent with the expected fibre structure of the steel sheet due to the working operations. Thus, the ductile cracking is attributed to an interaction of hydrogen with a slight metallurgical heterogeneity at the final stages of the ductile fracture.

4.8 Service implications

The results of the LIST in 3.5 wt% NaCl solution in Table 2 indicate that there was a small influence of hydrogen for the four MS-AHSS for the tests using a Pt counter electode. Furthermore, it is not expected for car components to be immersed in such salt solutions for an extended period of time in service. For the four steels, the yield strength decreases ranged from 3-6%; the decrease of fracture stress ranged from 4-7%; the HE index, values were not significantly different from zero, ranging from 0 to 3, except for the value of 10 for MS1500-Ezn-3; however this value may still be regarded as small with respect to HE susceptibility.

In the case of the experiment carried out using a carbon counter electrode, there was a somewhat greater influence of hydrogen on the fracture, and a somewhat decreased ductility. In both cases there was no indication of any subcritical crack growth associated with hydrogen.

The tests results at rapid stress rates in Table 4 indicate that hydrogen had minimal influence on MS-AHSS under conditions of rapid loading. Furthermore, high hydrogen fugacities may be expected to be rare in typical automotive service, particularly as hydrogen outgassing may be rapid.

4.9 Hydrogen concentration

4.9.1 Measured hydrogen concentration

Fig 21 compares the diffusible hydrogen concentration, C_{DH}, from Fig. 16 and Table 5, to the hydrogen concentration, C_H, evaluated from the permeation transients, from Table 6. Fig. 21 indicates that the hydrogen concentration, C_H, evaluated from the permeation transients was significantly greater than the diffusible hydrogen concentration, C_{DH}, by a factor from 2 to 6. The hydrogen concentration evaluated from the permeation transients is expected to be the steady state hydrogen concentration during cathodic hydrogen charging. This hydrogen concentration was the starting concentration of the steel at the end of the charging, and some hydrogen was expected to be lost between the end of charging and the measurement of the diffusible hydrogen concentration. However, the diffusion model for these steels in Fig. 20 indicates that the amount of hydrogen lost was expected to be relatively small, and is not sufficient to explain the difference between these two different measures of hydrogen contents.

4.9.2 As-rolled steels

The low diffusible hydrogen content measured in the as-rolled specimens indicates that the as-rolled steels are essentially hydrogen-free. The manufacturing process does not introduce considerable amounts of hydrogen into the steel or the hydrogen rapidly egresses. This agrees with studies that indicated no significant hydrogen uptake after forming [36,75]. Of some concern are other post-fabrication processes that could introduce hydrogen such as acid cleaning and electroplating.

4.9.3 Charging in 0.1 M NaOH

The hydrogen concentration increased with more negative overpotential in Fig. 16 in that the hydrogen concentration increased from the concentration for charging at -1248 mV_{SCE} (-1002 mV_{SHE}) to that charging at -1848 mV_{SCE} (-1602 mV_{SHE}). This is consistent with expectations [55,76].

The higher hydrogen concentration for cathodic charging at -1548 mV_{SCE} (-1302 mV_{SHE}), was unexpected, and there is no explanation. This may be related to the measurement technique, as the hydrogen concentration as measured from the permeation transients increased continuously with increasing overpotential, as expected, see Fig. 21.

4.9.4 Immersion in 3.5 wt% NaCl and 0.1 M HCl

Fig. 16 indicates that the hydrogen content after immersion in the 3.5 wt% NaCl solution at E_{corr} was measureable, and significantly greater than in the as-received steel. This indicates that some hydrogen is liberated at the specimen surface and some hydrogen enters the steel during corrosion at the free corrosion potential. Moreover, the amount of hydrogen was substantially higher for immersion in 3.5 wt% NaCl solution at E_{Zn}, consistent with expectations that the more negative applied potential will produce more hydrogen at the steel surface.

Conder et al [63] studied low carbon martensitic steels, similar to MS-AHSS. They charged the LCMS (yield strength 1150 MPa) for 24 hrs in 3.5 wt% NaCl at -900 mV_{SCE} (-654 mV_{SHE}). Their test was quite similar to the current test that involved MS1500 (yield strength of 1200 MPa) charged in 3.5 wt% NaCl at E_{Zn} (-752 mV_{SHE}). Conder et al measured a total hydrogen content of 0.8 ppm in the steel using hot melt extraction, whilst the measured diffusible hydrogen content in this work was substantially lower at 0.03 μg/g (ppm).

The relatively higher hydrogen uptake in HCl at E_{corr} is not surprising. In acidic conditions, hydrogen comes from the reduction of H^+ and water in the solution as a by-product of the corrosion reaction [77]. These cathodic reduction processes are dependent on the abundance of H^+, and therefore on pH. The acid can also breakdown oxide films formed at the steel surface, and this would also enhance hydrogen uptake [78]. Furthermore, hydrogen absorption of steels in an acidic solution is influenced by alloying elements [75]. For example, Cu can retard hydrogen absorption, while P, S, As, Se, Sb and Sn can enhance this effect.

4.9.5. Steel strength

The hydrogen uptake of AHSS is known to be influenced by the alloying elements, process history and microstructure. Loidl et al [37] studied several MS-AHSS, and compared the diffusible hydrogen concentration in charged specimens subjected to the slow strain rate test (SSRT). They found that the diffusible hydrogen concentration decreased with increasing tensile strength. This was attributed to the ability of dislocation to move and carry hydrogen. Stronger steels have lower dislocation mean free paths, and consequently have lower hydrogen concentrations for the same charging conditions. In the current study, the lowest hydrogen concentrations were also mostly measured in MS1500, but the expected trends for MS1300 and MS980 did not appear. This indicated that there was no clear relationship between diffusible hydrogen concentration and tensile strength of MS-AHSS. One factor that may have caused the difference in the results of the two studies is the charging condition. The study by Loidl et al tested hydrogen content from specimens subjected to the SSRT. This means that hydrogen charging of the specimens was done simultaneously with plastic deformation. In contrast, the current study did not apply stress during charging for the specimens whose hydrogen concentration was measured. The presence of stress or strain in the steel increases the hydrogen concentration [79,80].

4.10 Hydrogen permeation

The values of the hydrogen diffusion coefficient, D_{eff}, measured in this work, Table 6, are within the known scatterband for martensitic steels [81]. At room temperature, the reported values can range from 1 x 10^{-7} to 1 x 10^{-5} cm^2/s. The hydrogen diffusion coefficient in steels can be reduced by the presence of hydrogen traps [82]. Crystalline defects (e.g. dislocations, grain boundaries, phase boundaries, etc) are common hydrogen traps. Since hydrogen traps could be expected to increase with increasing tensile strength, it could be expected that the measured hydrogen diffusion coefficient, D_{eff}, would decrease from MS980 to MS1500. However, Table 6 indicates that the values of the hydrogen diffusion coefficient were similar for all three steels. This indicates that D_{eff} was not strongly influenced by the tensile strength nor by the metallurgical differences (e.g. fraction of ferrite to martensite). The higher values of D_{eff} at the more negative potentials may be attributed to a decreasing trapping effect [54,56]. During charging, hydrogen first occupies and fills the traps. With increasingly negative applied potential, the hydrogen fugacity is increased, more of the traps

are filled and the effective diffusion coefficient approaches the value of the lattice diffusion coefficient.

5.0 CONCLUSIONS

1. There was minimal influence of hydrogen for the four MS-AHSS in the LIST in 3.5 wt% NaCl, under the conditions used in this study.

2. There was minimal influence of hydrogen for hydrogen-precharged MS1300 and MS1500 subjected to tensile tests at substantial stress rates, under the conditions used in this study.

3. The hydrogen content of MS980, MS1300 and MS1500 increased with increasingly negative applied potential and the type of electrolyte. However, there was no clear correlation between the mechanical strength and hydrogen concentration.

4. There was no significant difference between the diffusivity of hydrogen in MS980, MS1300 and MS1500.

5. The use of a Pt counter electrode during cathodic hydrogen charging in 0.1 M NaOH decreased by ~70% the steady state hydrogen content of MS1500 compared with the case of a carbon, C, counter electrode) attributed to the Pt plating onto the specimen surface.

ACKNOWLEDGEMENTS

This research is supported by the Baosteel-Australia Joint Research & Development Centre (BAJC) Grant, BA13037, with linkage to Baoshan Iron and Steel Co., Ltd of China.

The authors also acknowledge the facilities, and the scientific and technical assistance, of the Australian Microscopy & Microanalysis Research Facility at the Centre for Microscopy and Microanalysis, The University of Queensland.

APPENDIX A – Counter electrodes

The current study used Pt as the counter electrode for electrolytic hydrogen charging. However, Pt may dissolve at a sufficiently oxidizing potential [57]. The XPS analysis did detect Pt on the steels cathodically charged in 0.1 M NaOH at -1700 $mV_{Hg/HgO}$ (-1602 mV_{SHE}) but no Pt was detected for steels cathodically chaged in 3.5 wt% NaCl at a lower overpotential. This implies that Pt in the 0.1M NaOH was oxidized to Pt ions at the relatively high anodic potential at the counter electrode, the Pt ions migrated to the working electrode, and Pt was plated out onto the steel electrode at the negative applied potential. Pt is a known to influence the hydrogen evolution reaction [83]. Hence any Pt deposited on the steel surface may influence hydrogen uptake by the steel and hydrogen permeation through the steels.

Consequently, the performance of alternative counter electrodes were examined: (i) graphite (C), and (ii) mixed metal oxide-coated titanium (MMO-Ti) (obtained from NMT Electrodes (Australia) Pty Ltd, Canning Vale, Western Australia). The MMO-Ti electrodes are becoming increasingly popular in impressed current cathodic protection systems.

Fig. A1 shows the hydrogen permeation current density through a MS1500 specimen as a function of time during cathodic charging in 0.1 M NaOH at -1700 $mV_{Hg/HgO}$ (-1602 mV_{SHE}) on the input side, carried out under identical conditions, except that the counter electrode used was Pt, C, or a MMO-Ti counter electrode. The Pt counter electrode was arranged as for the results described in the Tables 2, 4-6. In contrast, in the experiments using a C or MMO-Ti counter electrode, the counter electrode was placed in a separate counter electrode compartment, ~10 cm from the working electrode; and the counter electrode compartment was separated from the main charging solution by a frit to prevent solution mixing by convection.

For the experiment with the Pt counter electrode, the hydrogen permeation current density increased slowly over a period of 36 h to a maximum value and then slowly decreased somewhat. This behaviour is consistent with our prior measurements [54,55] and to literature observations [56,85], and is attributed to a slow conditioning of the surface which converts the surface iron oxides to a stable condition.

For the experiment with the C counter electrode, the permeation current density also increased slowly over the first 24 h, and was thereafter essentially constant, at a value

significantly larger than the steady state permeation current density with the Pt counter electrode.

For the experiment with the MMO-Ti counter electrode, the permeation current density continued to increase for over 84 h to much higher values.

Table A1 presents the results from a sequence of permeation decay transients similar to those in Table 6 and Fig. 17, and in particular presents the values for the measured steady-state permeation current density, i_{∞}, the effective diffusion coefficient, D_{eff}, and the hydrogen concentration, C_{H}, in the steel on the input side of the steel permeation specimen.

For the experiments with the Pt and C counter electrodes, these results indicate that the values of the effective diffusion coefficient, D_{eff}, were the same within experimental error, and the same as the values of the effective diffusion coefficient in Table 6, indicating that these electrodes had no influence on hydrogen diffusion inside the steel (which is to be expected) and furthermore that Pt had no influence on the hydrogen egress from the steel, and no influence on hydrogen entry process into the steel. However, the hydrogen concentration values indicated that there was substantially more hydrogen dissolved in the steel for identical cathode charging conditions when a C counter electrode was used compared with a Pt counter electrode. This indicates that a steel surface, on which there is some Pt, absorbs less hydrogen than an identical steel surface with no surface Pt.

The permeation experiment with the MMO-Ti counter electrode indicated that hydrogen content in the steel was significantly higher than for the experiment with the C counter electrode, and in addition, the values of the effective hydrogen diffusion coefficient were also somewhat higher. SEM examination of the MMO-Ti counter electrode revealed a cracked surface oxide, and EDS gave the following approximate concentration (in wt%): 26%Ti, 15%Ir, 13%Ru, 5%Ta, 1%Ca, and 38%O.

XPS analysis of the surface of the steel after permeation experiments with the MMO-Ti counter electrode indicated the presence on the steel surface of ruthenium metal (Ru), iridium (Ir) oxide, lead (Pb) oxide and cadmium (Cd) oxide. The presence of Ru and Ir was consistent with the elements in the SEM-EDS analysis. Pb and Cd were not found in the EDS analysis of the MMO-Ti. However, these two elements were not detected in the XPS analysis of the steel cathodically charged with the platinum counter electrode, shown in Fig. 11, so it is reasonable that these may have also originated from the MMO-Ti.

Table A2 shows the chemical analysis of the electrolyte in the counter electrode chamber at different times of the permeation experiment with the MMO-Ti counter electrode as analysed by the Analytic Services Unit at the School of Agriculture and Food Sciences, The University of Queensland. There was an increase in the amount of Ir, Ru, Ta, Ti, Al, Pb, Si and K in the electrolyte. It is logical to assume that these elements leached out from the MMO-electrode during the test.

Fig. A1 and Table A1 indicate that the Pt counter electrodes (i) decreased by ~ 70% the steady state H uptake of MS1500 during cathodic charging in 0.1 M NaOH (compared with the case of a C counter electrode) and (ii) seemed to have little influence on hydrogen diffusion in the steel and hydrogen egress from the steel. There was nevertheless a substantial amount of hydrogen in the steel under these charging conditions. This means that Pt counter electrodes should be used with caution during hydrogen embrittlement studies involving cathodic hydrogen charging.

Similarly Fig. A1 and Table A1 indicate that MMO-Ti counter electrodes should be avoided in such studies.

REFERENCES

1. WorldAutoSteel. Advanced High-Strength Steels Application Guidelines V5.0. Published May 5, 2014. . Available from http://www.worldautosteel.org. Downloaded on July 7, 2014.
2. Automotive Applications Council. AHSS 101-The Evolving Use of Advanced High-Strength Steels for Automotive Application. 2011. Available from http://www.autosteel.org. Downloaded on April 20, 2014.
3. X. Zhu, Z. Ma, and L. Wang. Current Status of Advanced High Strength Steel for Auto-making and its Development in Baosteel. Available from http://www.baosteel.com. Downloaded on May 21. 2014.
4. ULSAB-AVC Consortium. ULSAB-AVC (Advanced Vehicle Concepts) Overview Report. Available from http://www.autosteel.org. Downloaded on April 12, 2014.
5. O. Bouaziz, H. Zurob, and M. Huang, Driving Force and Logic of Development of Advanced High Strength Steels for Automotive Applications, Steel Research Int. 84:10 (2013) 937-947.
6. ArcellorMittal. Usibor: Steels for Hot Stamping. Available from http://fce.arcelormittal.com. Downloaded on April 12, 2014.
7. R.Z. Mallen, S. Tarr, and J. Dykeman. Recent Applications of High Strength Steels in North American Honda Production, Great Designs in Steel Seminar. Michigan, USA. Apr, 2008. Available from http://www.autosteel.org. Downloaded on July 22, 2014.
8. I. Han. Advanced High-Strength Steel Technologies in the 2014 Chevy Spark, General Motors, Great Designs in Steel 2014. Michigan, USA. May 2014. Available from http://www.autosteel.org. Downloaded on Oct 12, 2014.
9. R.P. Gangloff. Hydrogen assisted cracking of high strength alloys, in Comprehensive structural integrity Vol. 6, Environmentally Assisted Fracture. I. Milne, R.O. Ritchie, and B. Karihaloo, (Eds). 2003. Elsevier. pp. 31 - 101.
10. S. Lynch, Hydrogen embrittlement phenomena and mechanisms, Corros. Rev. 30 (2012) 105-123.
11. S. Ramamurthy and A. Atrens, Stress corrosion cracking of high-strength steels, Corros. Rev. 31:1 (2013) 1-31.
12. S. Ramamurthy and A. Atrens, The influence of applied stress rate on the stress corrosion cracking of 4340 and 3.5NiCrMoV steels in distilled water at 30 °C, Corros. Sci. 52:2 (2010) 1042-1051.
13. J.Q. Wang, A. Atrens, D.R. Cousens, P.M. Kelly, C. Nockolds, and S. Bulcock, Measurement of grain boundary composition for X52 pipeline steel, Acta Mater. 46:5677-5687 (1998).
14. A. Atrens and Z.F. Wang, ESEM observations of SCC initiation for 4340 high strength steel in distilled water, J Mater. Sci. 33 (1998) 405-415.
15. A. Oehlert and A. Atrens, SCC Propagation in Aermet 100, J. Mater. Sci. 33 (1998) 775-781.
16. R.M. Rieck, A. Atrens, and I.O. Smith, The Role of Crack Tip Strain Rate in the Stress Corrosion Cracking of High Strength Steels in Water, Met. Trans 20A (1989) 889-895.
17. Q. Liu and A. Atrens, A critical review of the influence of hydrogen on the mechanical properties of medium strength steels, Corros. Rev. 31 (2013) 85-104.
18. L. Duprez, K. Verbeken, and M. Verhaege. Effect of hydrogen on the mechanical properties of multiphase high strength steels, in Proceedings of Effects of hydrogen on materials: Proceedings of the 2008 International Hydrogen Conference. 2009. Grand Teton National Park, WY, USA.

19. T. Depover, L. Duprez, K. Verbeken, E. Wallaert, and M. Verhaege. In-situ mechanical evaluation of hydrogen embrittlement for TRIP, FB, DP and HSLA steels, in Proceedings of Steely Hydrogen Conference. 2011. Ghent Belgium.
20. T. Depover, D. Escobar, E. Wallaert, Z. Zermout, and K. Verbeken, Effect of hydrogen charging on the mechanical properties of advanced high strength steels, Int. J. Hydrogen Energ. 39:9 (2014) 4647-4656.
21. D. Pérez Escobar, C. Miñambres, L. Duprez, K. Verbeken, and M. Verhaege, Internal and surface damage of multiphase steels and pure iron after electrochemical hydrogen charging, Corros. Sci. 53:10 (2011) 3166-3176.
22. F.J. Recio, M.C. Alonso, L. Gaillet, and M. Sánchez, Hydrogen embrittlement risk of high strength galvanized steel in contact with alkaline media, Corros. Sci. 53:9:9 (2011) 2853-2860.
23. M. Koyama, E. Akiyama, and K. Tsuzaki, Hydrogen embrittlement in a Fe-Mn-C ternary twinning-induced plasticity steel, Corros. Sci. 54 (2012) 1-4.
24. N.E. Nanninga, Y.S. Levy, E.S. Drexler, R.T. Condon, A.E. Stevenson, and A.J. Slifka, Comparison of hydrogen embrittlement in three pipeline steels in high pressure gaseous hydrogen environments, Corros. Sci. 59 (2012) 1-9.
25. H.F. Jackson, K.A. Nibur, C. San Marchi, J.D. Puskar, and B.P. Somerday, Hydrogen-assisted crack propagation in 304L/308L and 21Cr–6Ni–9Mn/308L austenitic stainless steel fusion welds, Corros. Sci. 60 (2012) 136-144.
26. A. Nagao, C. Smith, M. Dadfarnia, P. Sofronis, and I.M. Robertson, The role of hydrogen in hydrogen embrittlement fracture of lath martensitic steel, Acta Materialia 60:13–14 (2012) 5182-5189.
27. T. Doshida, M. Nakamura, H. Saito, T. Sawada, and K. Takai, Hydrogen-enhanced lattice defect formation and hydrogen embrittlement of cyclically prestressed tempered martensitic steel, Acta Mater. 61:20 (2013) 7755-7766.
28. M. Koyama, C.C. Tasan, E. Akiyama, K. Tsuzaki, and D. Raabe, Hydrogen-assisted decohesion and localized plasticity in dual-phase steel, Acta Mater. 70 (2014) 174-187.
29. M. Hatano, M. Fujinami, K. Arai, H. Fujii, and M. Nagumo, Hydrogen embrittlement of austenitic stainless steels revealed by deformation microstructures and strain-induced creation of vacancies, Acta Mater. 67 (2014) 342-353.
30. I. Park, S. Jo, M. Kang, S. Lee, and Y. Lee, The effect of Ti precipitates on hydrogen embrittlement of Fe–18Mn–0.6C–2Al–xTi twinning-induced plasticity steel, Corros. Sci. 89 (2014) 38-45.
31. I. Park, S. Lee, H. Jeon, and Y. Lee, The advantage of grain refinement in the hydrogen embrittlement of Fe–18Mn–0.6C twinning-induced plasticity steel, Corros. Sci. 93 (2015) 63-69.
32. W.M. Garrison Jr. and N.R. Moody. Hydrogen embrittlement of high strength steels, in Gaseous hydrogen embrittlement of materials in energy technologies. R.P. Gangloff and B.P. Somerday, (Eds). 2012. Woodhead Publishing. pp. 421-484.
33. G. Wang, Y. Yan, J. Li, J. Huang, Y. Su, and L. Qiao, Hydrogen embrittlement assessment of ultra-high strength steel 30CrMnSiNi2, Corros. Sci.:77 (2013) 273-280.
34. L.P.M. Santos, M. Béreš, I.N. Bastos, S.S.M. Tavares, H.F.G. Abreu, and M.J. Gomes da Silva, Hydrogen embrittlement of ultra high strength 300 grade maraging steel, Corros. Sci. 101 (2015) 12-18.
35. C. Willan. Hydrogen Embrittlement A Historical Overview. Available from www.omegaresearchinc.com/. Downloaded on July 1, 2014.

36. G. Lovicu, M. Bottazzi, F. D'Aiuto, M. De Sanctis, A. Dimatteo, C. Santus, and R. Valentini, Hydrogen embrittlement of automotive advanced high-strength steels, Metall. Mater. Trans. A. 43 (2012) 4075-4087.
37. M. Loidl, O. Kolk, S. Veith, and T. Gobel, Characterization of hydrogen embrittlement in automotive advanced high strength steels, Mat.-wiss. u.Werkstofftech 42:12 (2011).
38. J.A. Ronevich, J.G. Speer, and D.K. Matlock, Hydrogen embrittlement of commercially produced advanced high strength steels, SAE Int. J. Mater. Manuf. 3:1 (2010) 255-267.
39. J. Venezuela, Q. Liu, M. Zhang, Q. Zhou, and A. Atrens, The influence of hydrogen on the mechanical and fracture properties of some martensitic advanced high strength steels studied using the linearly increasing stress test, Corros. Sci. 99 (2015) 98-117.
40. A. Atrens, C.C. Brosnan, S. Ramamurthy, A. Oehlert, and I.O. Smith, Linearly increasing stress test (LIST) for SCC research, Meas. Sci. Technol. 4 (1993) 1281-1292.
41. J. Salmond and A. Atrens, SCC of copper using the linearly increasing stress test, Scripta Met. Mater. 26 (1992) 1447-1450.
42. E. Gamboa and A. Atrens, Stress corrosion cracking fracture mechanisms in rock bolts, J Mater. Sci. 38:18 (2003) 3813-3829.
43. A. Atrens, J.Q. Wang, K. Stiller, and H.O. Andren, Atom probe field ion microscope measurements of carbon segregation at an alpha:alpha grain boundary and service failures by intergranular stress corrosion cracking, Corros. Sci. 48 (2006) 79-92.
44. E. Villalba and A. Atrens, Metallurgical aspects of rock bolt stress corrosion cracking, Mater. Sci. Eng. A 491 (2008) 8-18.
45. N. Winzer, A. Atrens, W. Dietzel, G. Songa, and K.U. Kainer, Comparison of the linearly increasing stress test and the constant extension rate test in the evaluation of transgranular stress corrosion cracking of magnesium, Mater. Sci. Eng. A 472:1-2 (2008) 97-106.
46. E. Villalba and A. Atrens, Hydrogen Embrittlement and Rock Bolt Stress Corrosion Cracking, Eng. Fail. Anal. 16 (2009) 164-175.
47. S. Ramamurthy, W.M.L Lau, and A. Atrens, Influence of the applied stress rate on the stress corrosion cracking of 4340 and 3.5NiCrMoV steels under conditions of cathodic hydrogen charging, Corrosion Science 53:7 (2011) 2419-2429.
48. Q. Liu, B. Irwanto, and A. Atrens, The Influence of Hydrogen on 3.5NiCrMoV steel studied using the linearly increasing stress test. , Corros. Sci. 67 (2013) 193-203.
49. Q. Liu, B. Irwanto, and A. Atrens, Influence of hydrogen on the mechanical properties of some medium-strength Ni–Cr–Mo steels, Mater. Sci. Eng. A 617 (2014) 200-210.
50. F. Cao, Z. Shi, G. Song, M. Liu, M. Dargusch, and A. Atrens, Stress corrosion cracking of several solution heat-treated Mg–X alloys, Corros. Sci. 96 (2015) 12-132.
51. Q.J. Zhou, L. Wang, and J.X. Li. Experimental study on delayed fracture of TS 980 MPa grade steels for automotive applications, in Proceedings of 2nd International Conference on Metals and Hydrogen. May 5-7, 2014. Ghent, Belgium.
52. C.D. Horvath and B. Oxley. A Practical and Effective Test for Rank Ordering Advanced High-Strength Steels Based on Their Sensitivity to Hydrogen Embrittlement, in Proceedings of Great Designs in Steel 2015. May 2015. Livonia, Mich.
53. M.A.V. Devanathan and Z.Stachurski, The mechanism of hydrogen evolution in iron in acid solutions by determination of permeation rates, J. Electrochem. Soc. 111 (1964) 619-623.

54. Q. Liu and A. Atrens, Reversible hydrogen trapping in a 3.5NiCrMoV medium strength steel, Corros. Sci. 96 (2015) 112-120.
55. Q. Liu, A. Atrens, Z. Shi, K. Verbeken, and A. Atrens, Determination of the hydrogen fugacity during electrolytic charging, Corros. Sci. 87 (2014) 239-258.
56. T. Zakroczymski, Adaptation of the electrochemical permeation technique for studying entry, transport and trapping of hydrogen in metals, Electrochim. Acta 51 (2006) 2261-2266.
57. R.P. Frankenthal and H.W. Pickering, Some considerations on the use of platinum electrodes in chloride solutions, J Electrochem. Soc. 112:5 (1965) 514-517.
58. D. Nolan and M. Pitrun, Diffusible Hydrogen Testing in Australia, 48:1-2 (2004) 14-20, Welding in the World 48:1-2 (2004) 1-20.
59. P. Delahay, M.Pourbaix, and P. Van Rysselberghe, Potential-pH diagrams, J Chem. Educ. 27 (1950) 683.
60. H.W. Walton. Ubiquitous hydrogen, in Proceedings of Heat treating: Including Steel Heat ing in the New Millenium. 1999. ASM Int.
61. C.D. Beachem, A new model for hydrogen assisted cracking (Hydrogen embrittlement), Metall. Trans. 3 (1972) 437 – 451.
62. H.K. Birnbaum, I.M. Robertson, and P. Sofronis. Hydrogen effects on plasticity, in Multiscale phenomena in plasticity. J. Lépinoux, (Ed). 2000. Kluwer Academic Pub. pp. 367 - 381.
63. R.J. Conder, P. Felton, R. Burke, and P. Dent, Hydrogen Embrittlement Testing Of High Strength Low Carbon Martensitic Steels, Corrosion 2015, NACE International, San Antonio, Texas. 2010.
64. J.H. Payer, A.G. Preban, and H.P.Leckie, Hydrogen-stress cracking of low carbon martensitic steel, Corrosion 32:2 (1976) 52-56.
65. J. Crank, *The Mathematics of Diffusion, 2nd Ed*. Clarendon Press, Oxford, London. 1975.
66. C. Willan. The effects of acid cleaning on hydrogen embrittlement: Final report, Omega Research Inc. Available from omegaresearchinc.com, 28.08.1999. Available from. Downloaded on Sep 20, 2015.
67. M.R. Louthan Jr. Effects of hydrogen on the mechanical properties of low carbon and austenitic steels, in Hydrogen in Metals. I.M. Bernstein and A.W. Thompson, (Eds). 1974. American Society for Metals: Metals Park, OH. pp. 53-77.
68. T. Toh and W.M. Baldwin, *Stress Corrosion Cracking and Embrittlement*, ed. W.D. Robertson. J. Wiley and Sons, Inc., New York, USA. 1976.
69. R.E. Smallman and R.J. Bishop, *Modern Physical Metallurgy and Materials Engineering. 6th Ed.*, Elsevier Science Ltd., Woburn, MA, USA. 1999.
70. A. Turnbull. Test Methods for Environment-Assisted Cracking. National Physical Laboratory Report DMM(A)66: Teddington, Middlesex, UK (1992).
71. F. Zwettler, H. Duchaczek, D. Windischbaue, and A. Walter Hassel. Electrochemical loading and determination of hydrogen at Voestalpine, in Proceedings of 2nd International Conference on Metals and Hydrogen. May 5-7, 2014. Ghent, Belgium.
72. A. Oudriss, A. Fleurentin, E. Conforto, C. Berziou, C. Rebere, S. Conhendoz, C. Savall, J. Creus, J.M. Sobrino, and X. Feaugas. On the relationship of baking time and hydrogen embrittlement on martensitic steels, in Proceedings of 2nd International Conference on Metals and Hydrogen. May 5-7, 2014. Ghent, Belgium.
73. S.J. Lee, J.A. Ronevich, G. Krauss, and D.K. Matlock, Hydrogen embrittlement of hardened low-carbon sheet steel, ISIJ Int. 50:2 (2010) 294-301.
74. R.W. Balluffi, S.M. Allen, and W.C. Carter, *Kinetics of Materials*. John Wiley and Sons, Hoboken, NJ. 2005.

75. H.J. Grabke and E. Riecke, Absorption and diffusion of hydrogen in steels, Mater. Tehnol. 34:6 (2000) 331-342.
76. A. Atrens, D. Mezzanote, N. Fiore, and M. Genshaw, Electrochemical studies of hydrogen diffusion and permeability in Ni, Corros. Sci. 20 (1980) 673-684.
77. A. Turnbull, Perspectives on hydrogen uptake, diffusion and trapping, Int. J Hydrogen Energy 40:47 (2015) 16961-16970.
78. A. Turnbull. Hydrogen diffusion and trapping in metals, in Gaseous hydrogen embrittlement of materials in energy technologies: Mechanisms, Modelling and Future Developments. R.P. Gangloff and B.P. Somerday, (Eds). 2012. Woodhead Publishing: PA, USA. pp. 89-128.
79. T. Zakroczymski, The Effect of Straining on the Transport of Hydrogen in Iron, Nickel, and Stainless Steel, Corrosion 41:8 (1985) 485-489.
80. U. Hadam and T. Zakroczymski, Absorption of hydrogen in tensile strained iron and high-carbon steel studied by electrochemical permeation and desorption techniques, International Journal of Hydrogen Energy 34:5 (2009) 2449-2459.
81. T. Bollinghaus, H. Hoffmeister, and C. Middel, Scatterbands for hydrogen diffusion coefficients in steels having ferritic or martensitic microstructures and steels having an austenitic microstructure at room temperature, Welding in the World 37 (1996) 16-23.
82. I.M. Bernstein and G.M. Pressouyre. The role of traps in the microstructural control of hydrogen embrittlement of steels, in Hydrogen degradation of ferrous alloys. R.A. Oriani, J.P. Hirth, and M. Smialowski, (Eds). 1985. Noyes Publication: New Jersey, USA. pp. 641-685.
83. M. Pourbaix, *Atlas of electrochemical equilibria in aqueous solutions (English edition)*. Pergamon press, Oxford. 1966.
84. R.H. Jones. A review of combined impurity segregation-hydrogen embrittlement process, in Advances in the Mechanics and Physics of Surfaces - Vol 3. R.M. Latanision and T.E. Fischer, (Eds). 1986. Harwood Academic Publishers: New York, USA. pp. 1-60.
85. T. Zakroczymski and Z. Szklarska-Smialowska, Activation of the iron surface to hydrogen absorption resulting from a long cathodic treatment in NaOH solution J Electrochem. Soc. 132:11 (1985) 2548-2552.

Figure

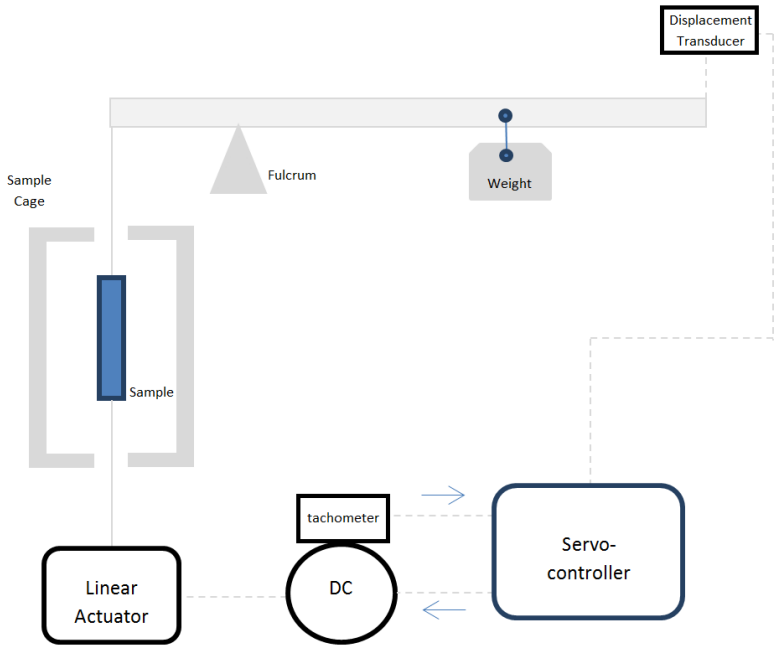

Fig. 1. Schematic of the Linear Increasing Stress Test (LIST) apparatus (adapted from Atrens et al [23]).

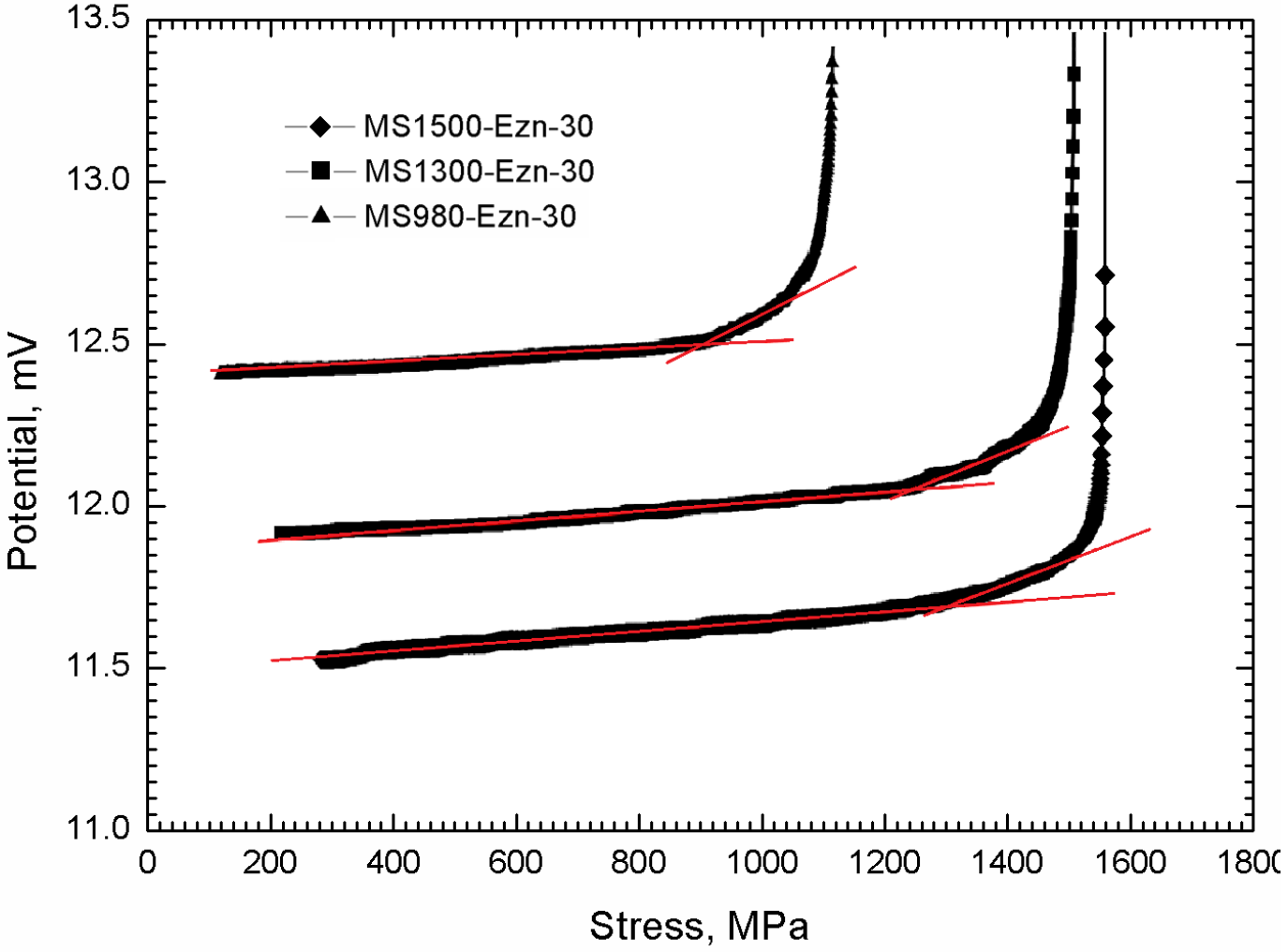

Fig. 2. Typical plot of potential drop versus applied stress. The plots have been displaced vertically somewhat to provide clear separation between the curves. The yield or threshold stress (σ_{TH}) was graphically determined at the transition point of the slope.

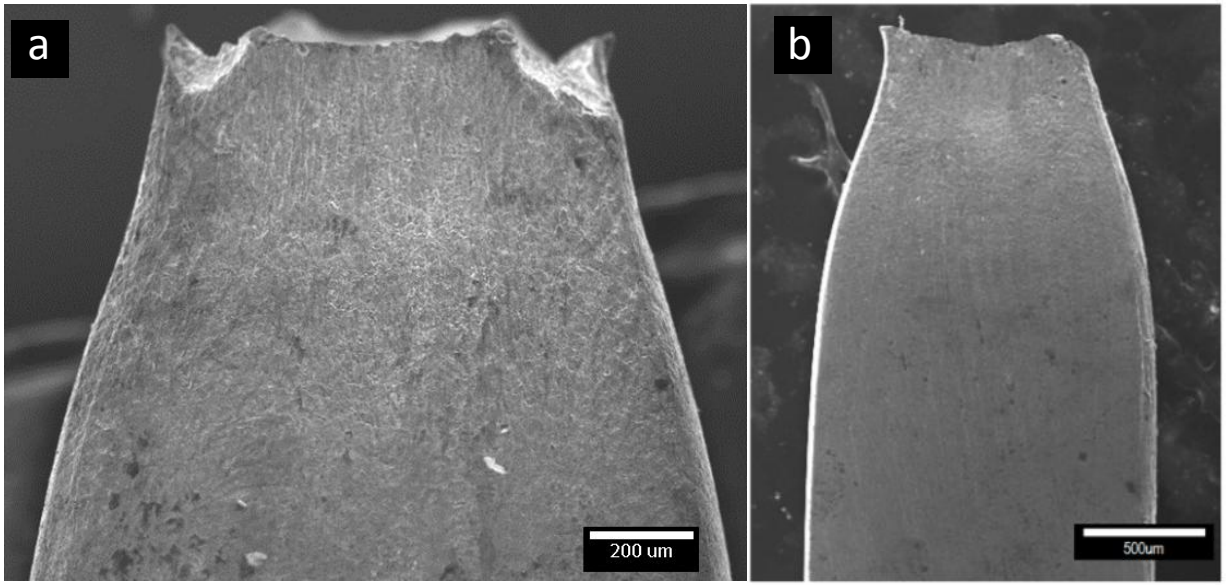

Fig. 3. SEM images of the typical cup-cone fracture viewed from the (a) broad and (b) short transverse sides. Sample: MS980 at 0.064 MPa s^{-1} at E_{Zn} (-752 mV_{SHE}) with Pt counter electrode.

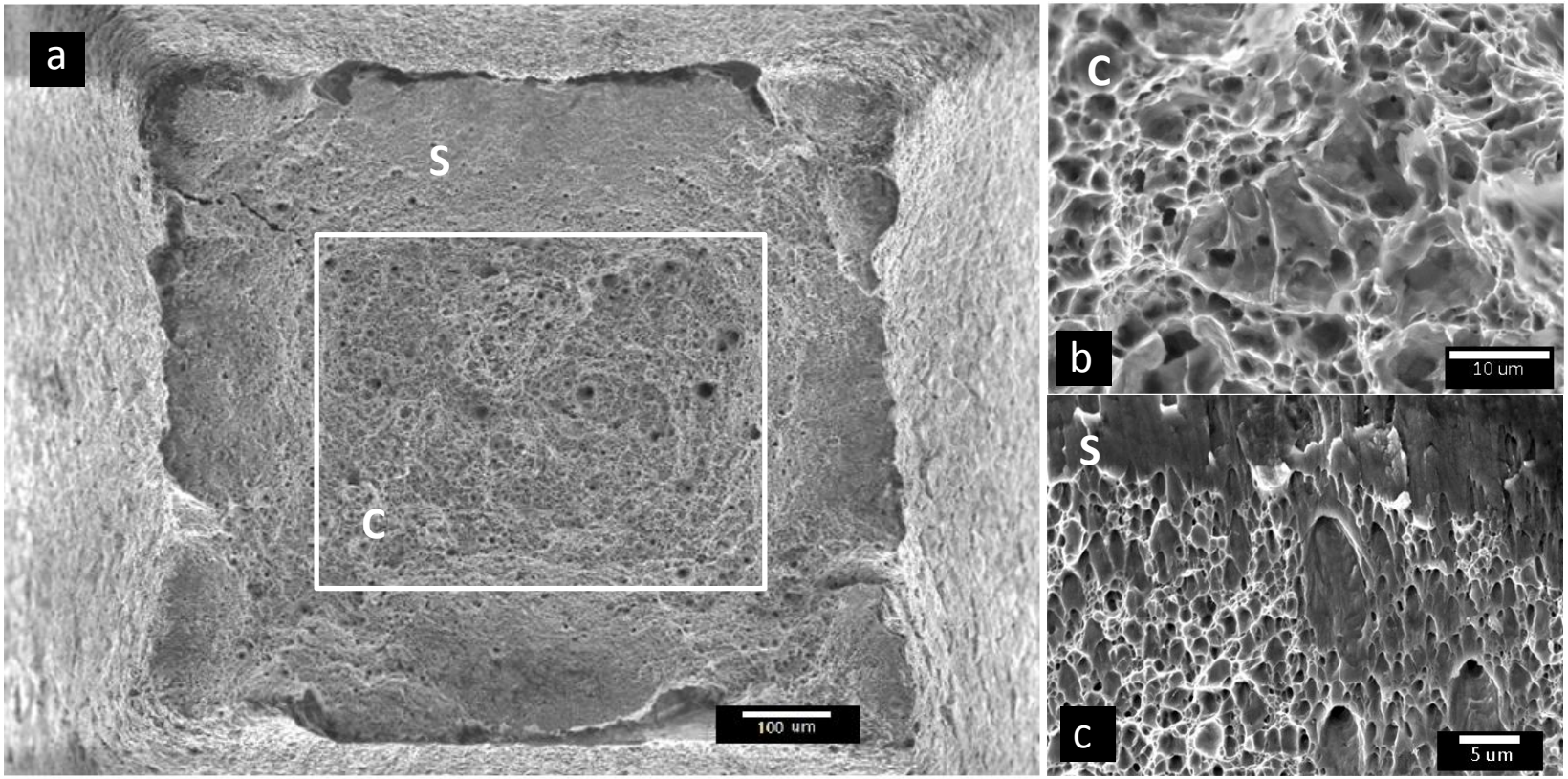

Fig. 4. Top view of a typical cup-cone fracture for MS-AHSS after LIST in 3.5% NaCl. The center (C) and the shear (S) regions lips showed the presence of microvoid coalescence dimples as presented in Figs. 4b and 4c. Sample: MS980 at 0.064 MPa s^{-1} at E_{Zn} (-752 mV_{SHE}) with Pt counter electrode.

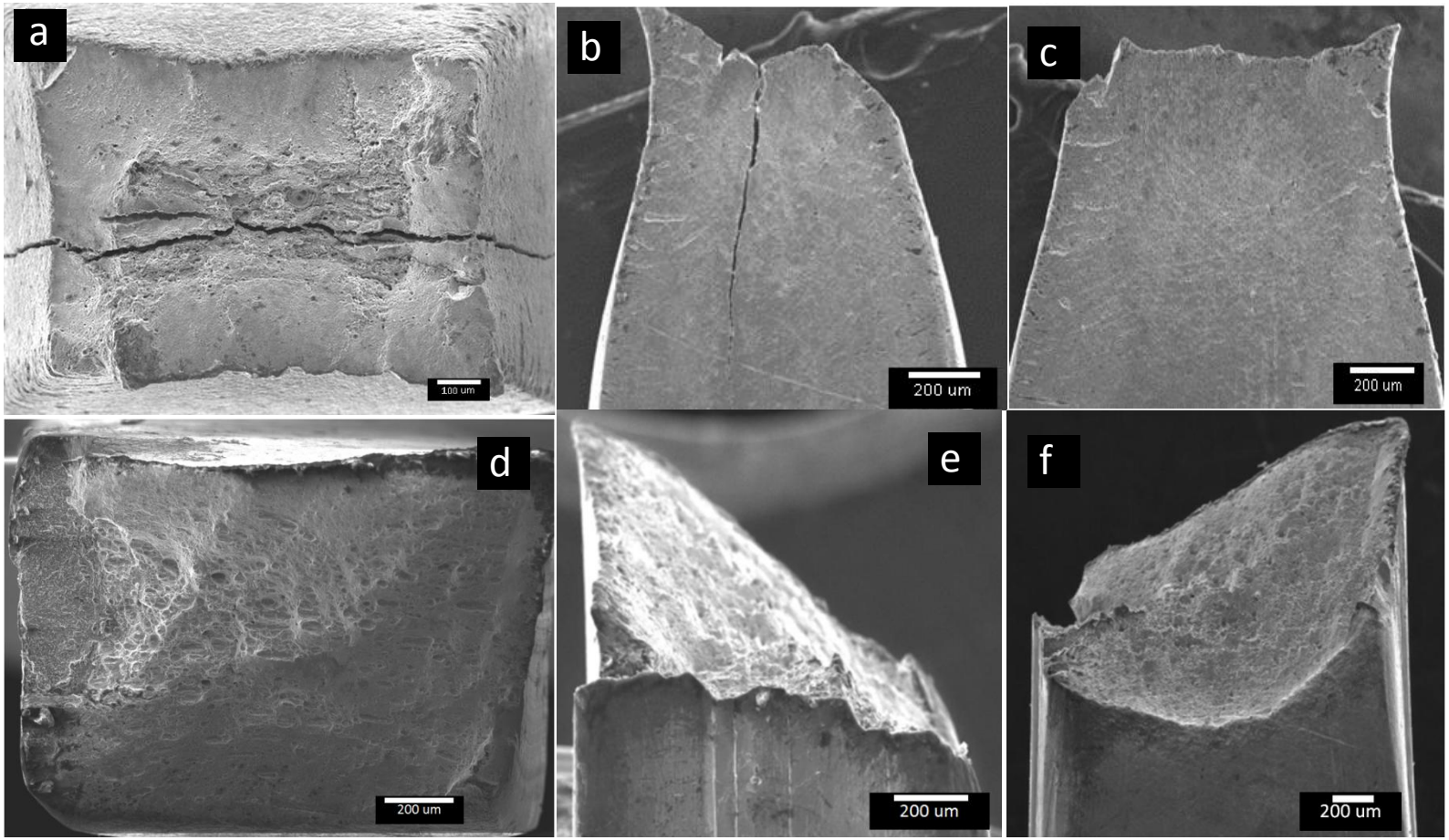

Fig. 5. SEM images of the fracture surface of the MS1500 at 0.0080 MPa s^{-1} at E_{Zn} (-752 mV_{SHE}) in 3.5% NaCl with Pt counter electrode: (a) top view, (b) short transverse side and (c) broad transverse side. SEM images of the fracture surface of the MS1500 at 0.0080 MPa s^{-1} at E_{Zn} (-752 mV_{SHE}) in 3.5% NaCl and using a graphite electrode: (d) top view, (e) short transverse side and (f) broad transverse side.

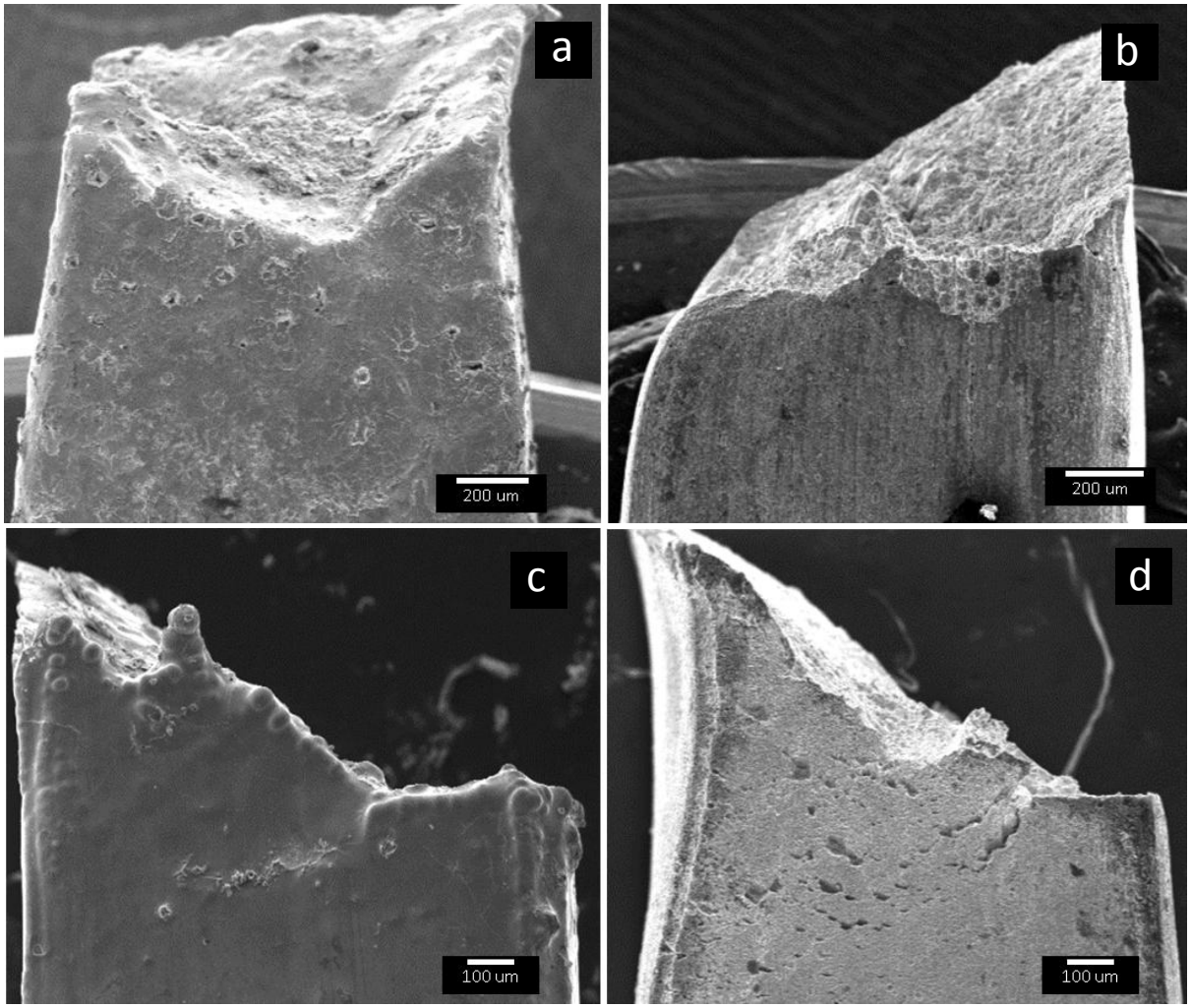

Fig. 6. The fracture surface of the MS980 (a and b) and MS1500 (c and d) after LIST at 0.0064 and 0.008 MPa s^{-1} in 0.1M HCl under uniform corrosion conditions .

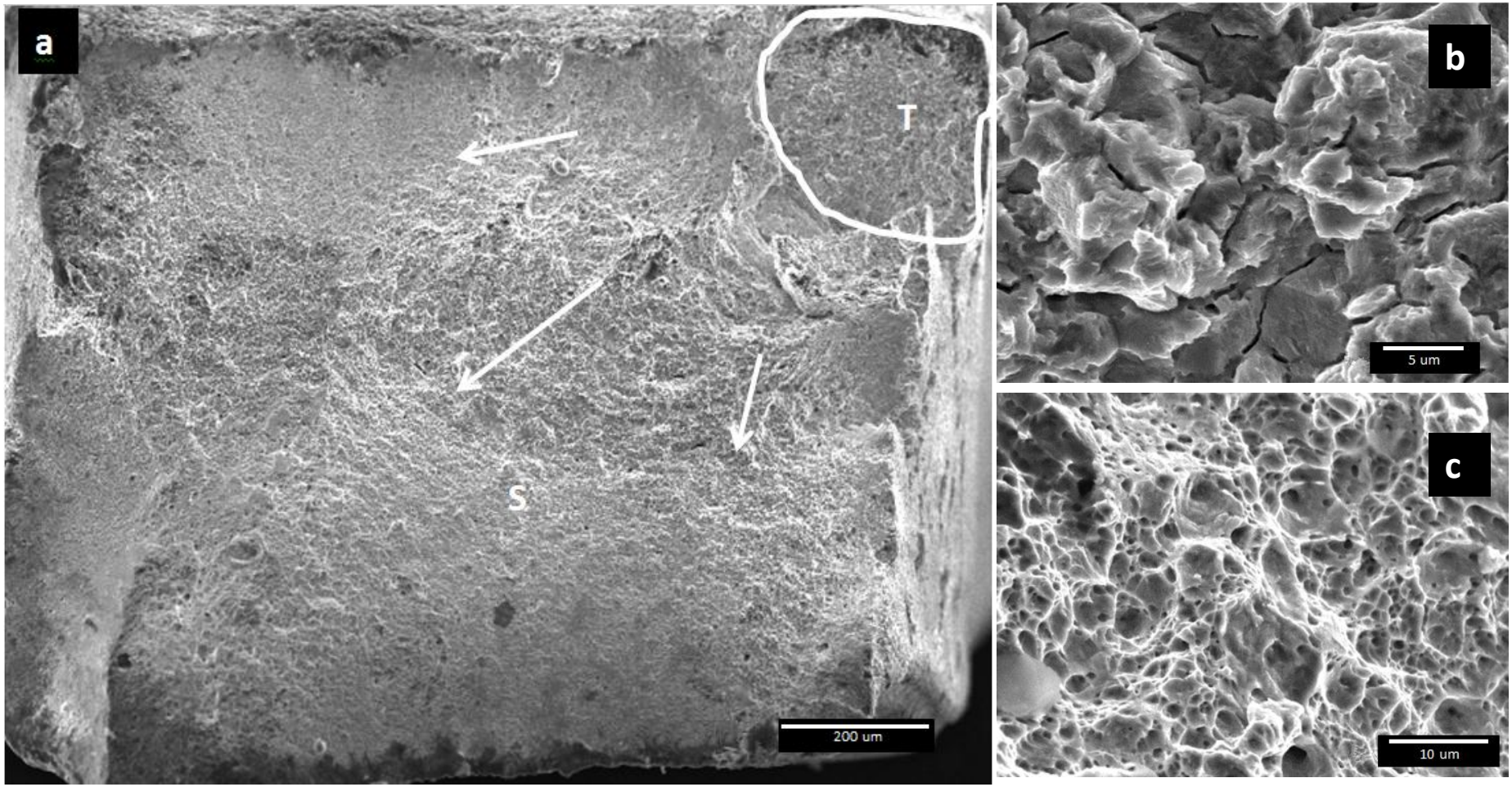

Fig. 7. (a) Typical SEM image of the fracture surface of the non-creviced MS1500 after LIST at 0.008 MPa s^{-1} in 0.1 M HCl. The 'T' region refers to crack nucleation region and 'S' is the crack propagation zone. The arrow refers to direction of crack growth. (b) Details of 'T' showing a mix of quasi-cleavage and intergranular fracture. (c) Close-up of region 'S' showing shear MVC dimples.

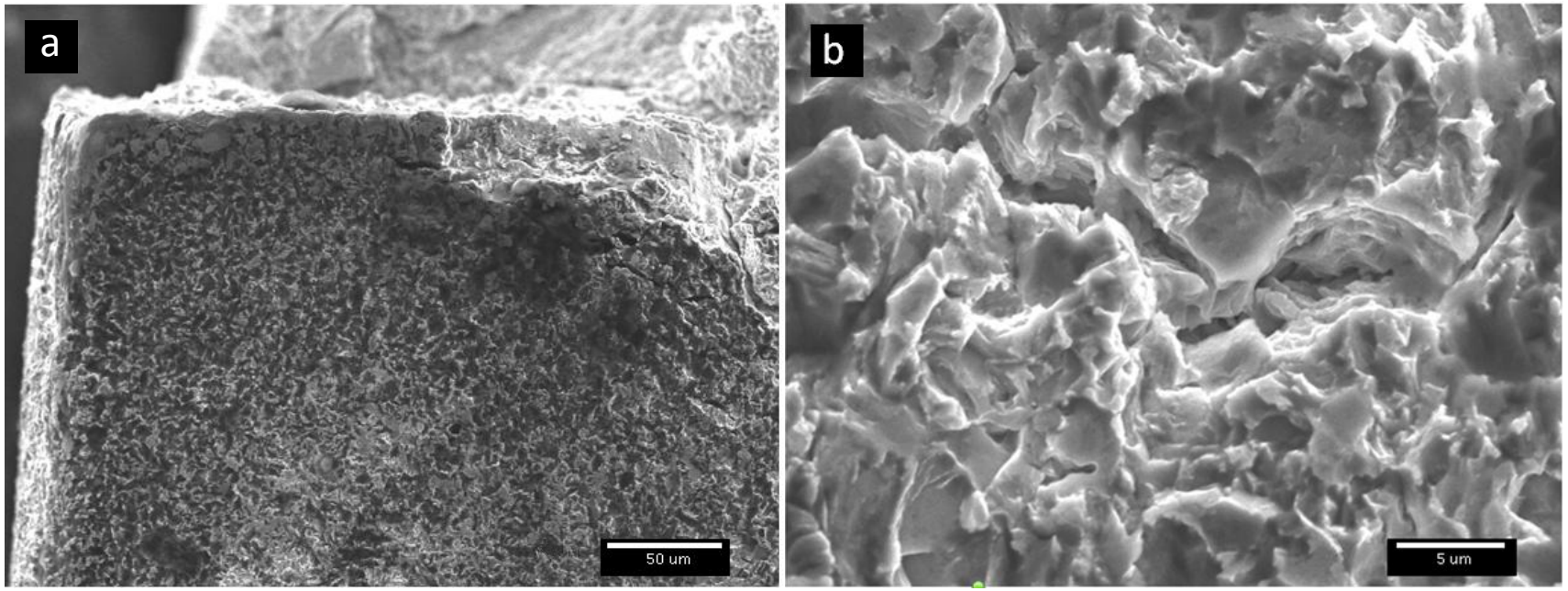

Fig. 8. (a) SEM image of the specimen surface of the non-creviced MS1500 after LIST at 0.008 MPa s^{-1} in 0.1 M HCl. (b) Close-up view of the surface showing rough features with superficial cracks.

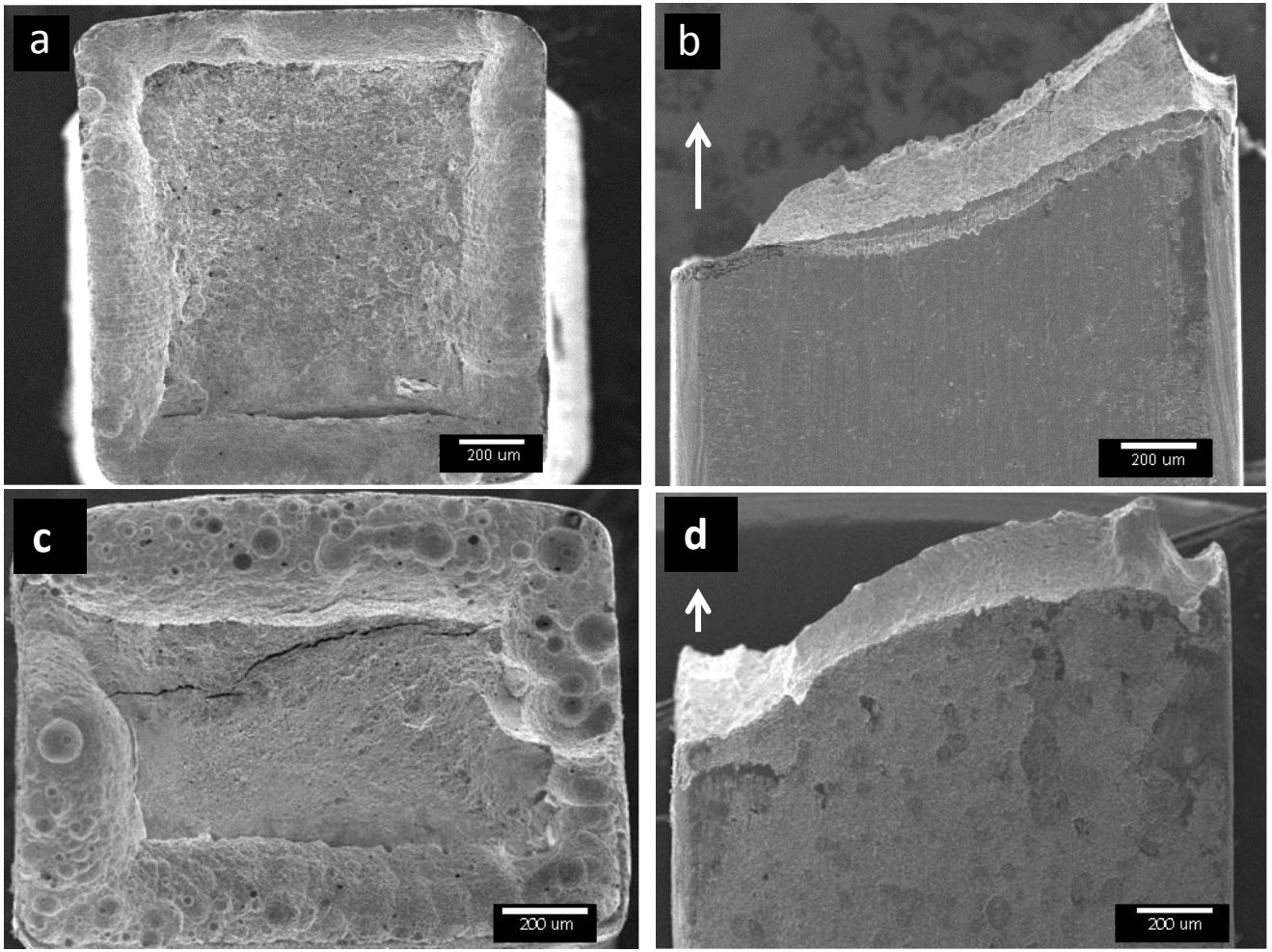

Fig. 9. SEM images of the creviced MS980 viewed (a) normal to the fracture surface and from the (b) transverse broad side. SEM images of the creviced MS1500 viewed (c) normal to the fracture surface and from (d) transverse broad side. Arrow shows direction of applied tensile load. (Testing conditions: LIST at 0.008 MPa s^{-1} in 0.1 M HCl)

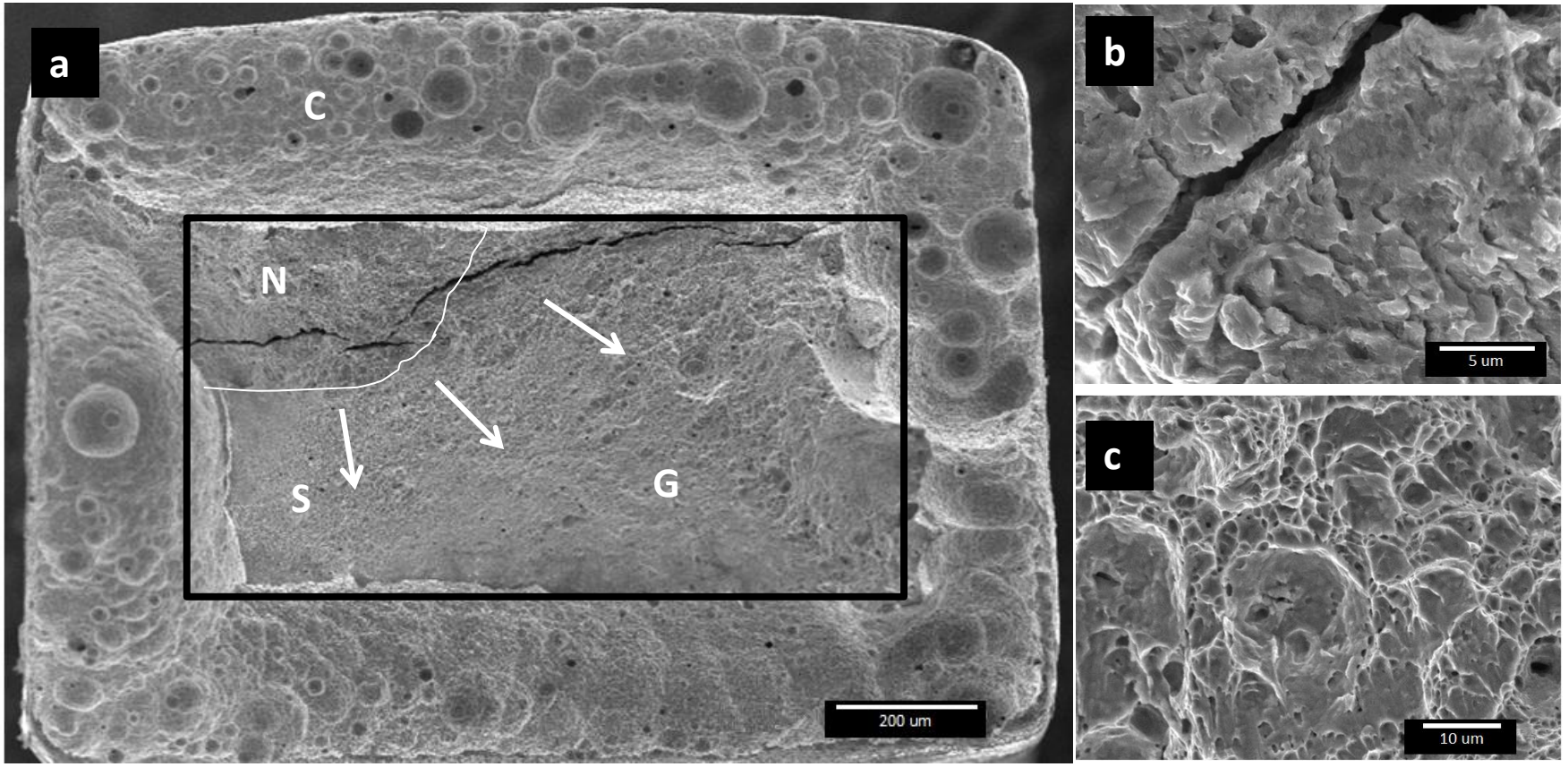

Fig. 10. (a) SEM image of the fracture surface of the creviced MS1500 after LIST at 0.008 MPa s^{-1} in 0.1 N HCl. The C region denotes areas which experienced crevice corrosion. Region 'S' is the area enclosed by the rectangle, and was to the final load-bearing area before fracture. Within region 'S,' area 'N' is to the crack nucleation area and 'G' is the crack propagation region. The arrows refer to the direction of crack growth. (b) Close-up of region N showing quasi-cleavage fracture. (c) Close-up of region G showing shear dimples.

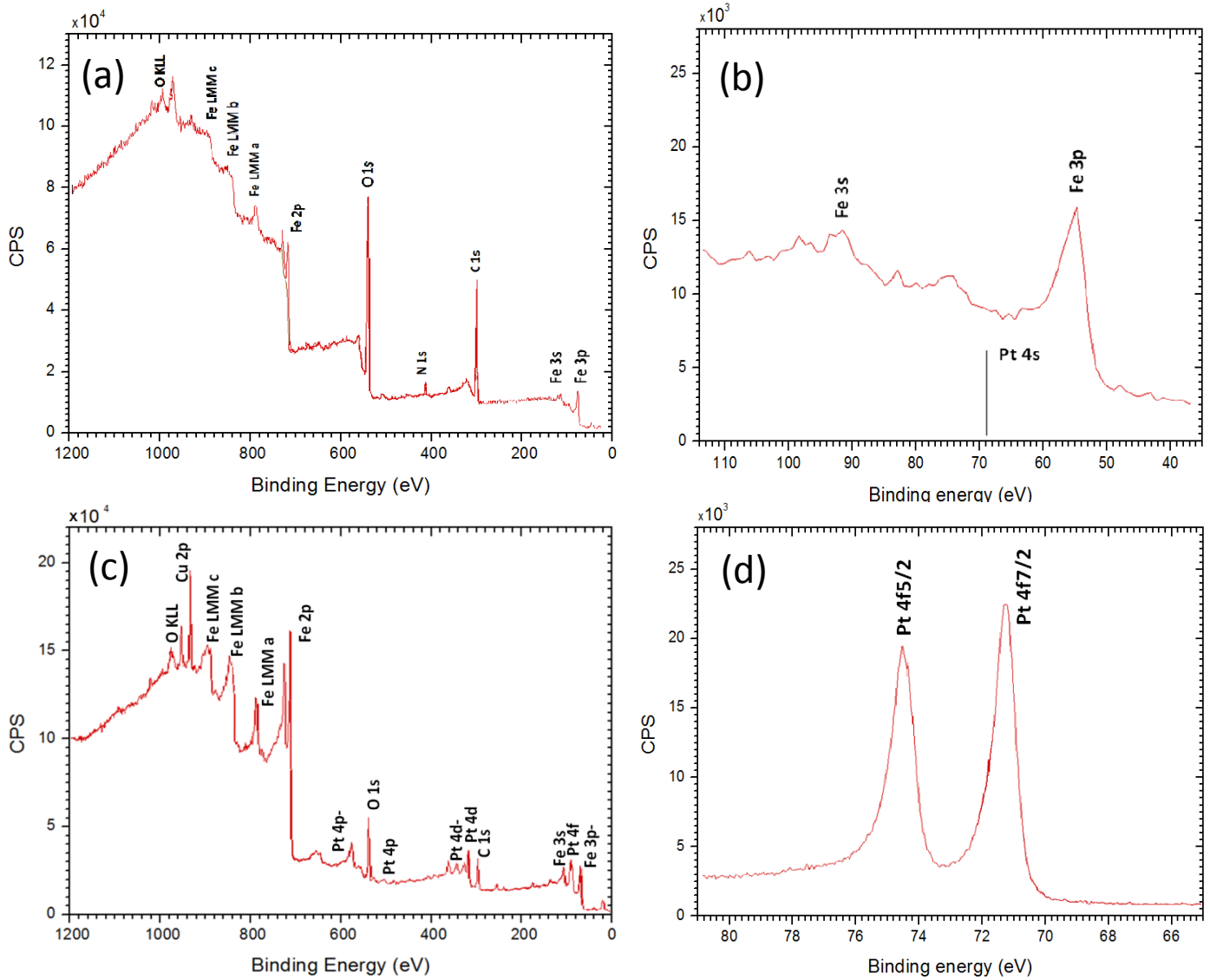

Fig. 11. (a) XPS survey scan indicated the absence of Pt on the MS1180 specimen charged at E_{Zn} (-752 mV_{SHE}) in 3.5 wt% NaCl for a total of 4 d, and (b) corresponding high resolution scan showing where Pt peak is expected if present (binding energy 71 eV). (c) XPS survey scan and (d) high resolution scan showing the presence of Pt on MS1180 charged at -1700 $mV_{Hg/HgO}$ (-1602 mV_{SHE}) in 0.1 M NaOH at the slowest applied stress rate (3 rph) for a total of 4 d.

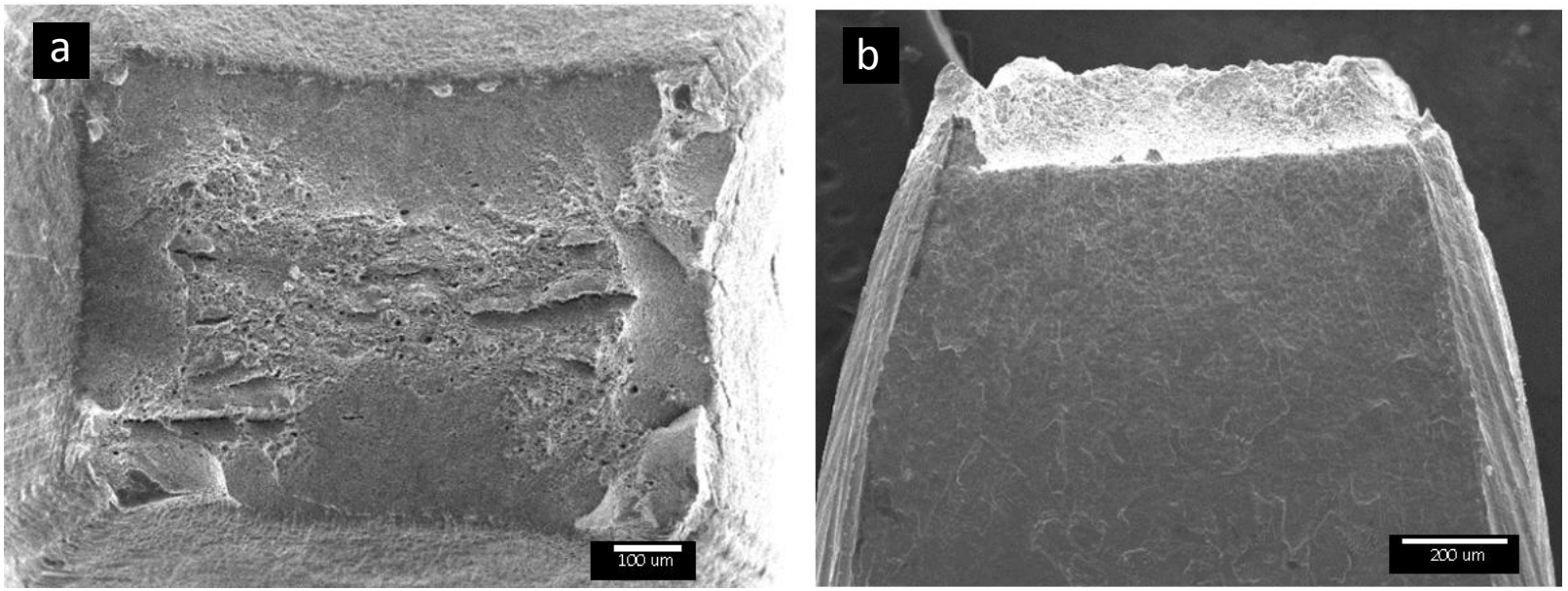

Fig. 12. SEM images of a typical fractured steel specimen subjected to 10 min holding time test after charging in 0.1 M NaOH viewed from (a) top, and (b) broad transverse side. Fracture mode is cup-cone, and the fracture surface possessed the typical central and shear lip region associated with ductile behaviour. (Specimen MS1500-10min-30: MS1500 subjected to LIST at 0.080 MPa s^{-1})

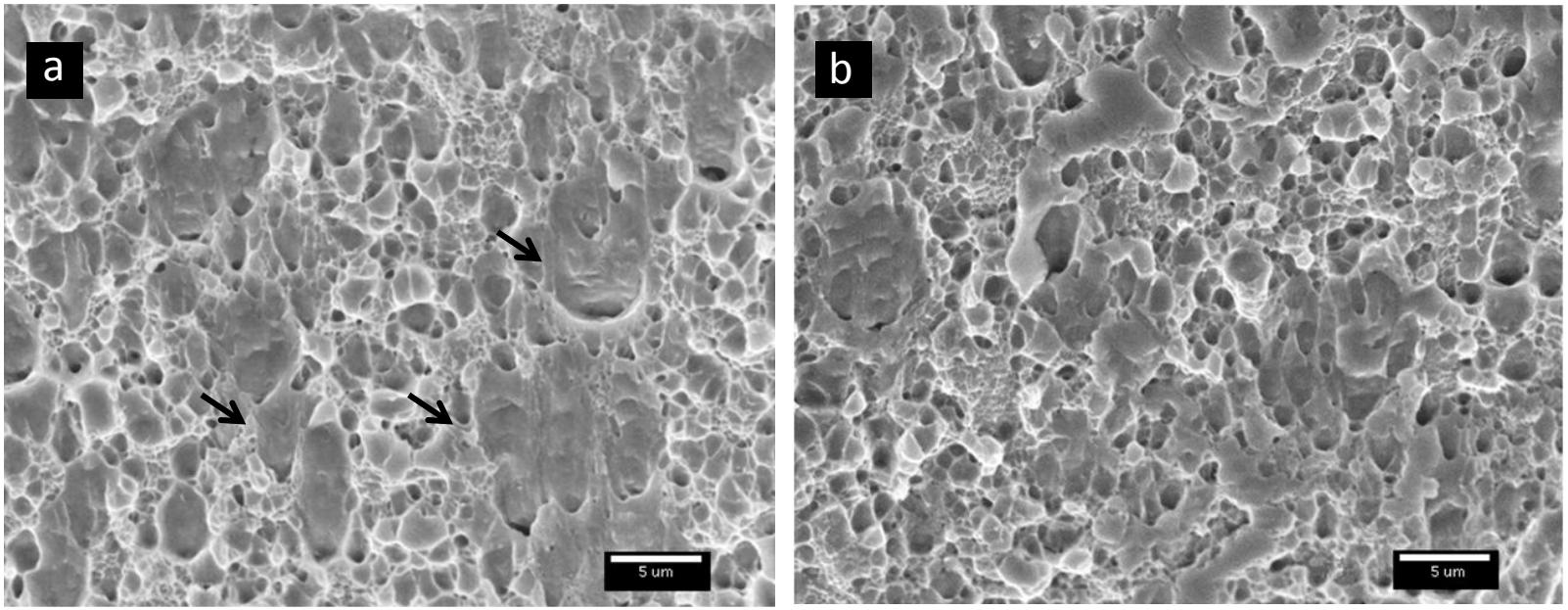

Fig. 13. SEM images of the shear lip region from (a) uncharged and (b) hydrogen-charged MS1300 subjected to the conventional tensile test. The uncharged specimen possessed larger, deeper and more elongated shear dimples. Arrows point to highly extended parabolic MVC dimples.

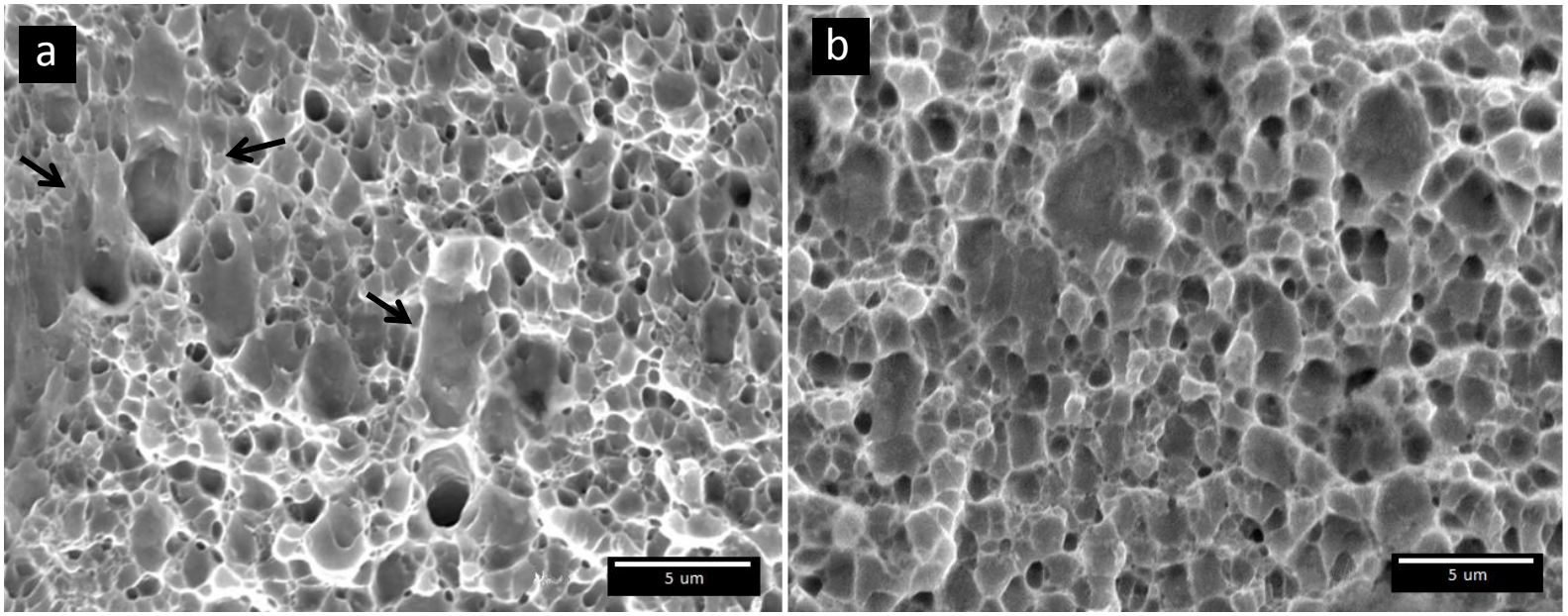

Fig. 14. SEM images of the shear lip region from (a) uncharged and (b) hydrogen-charged MS1500 subjected to the conventional tensile test. The uncharged specimen displayed larger, deeper and more elongated shear dimples. Arrows point to highly extended parabolic MVC dimples.

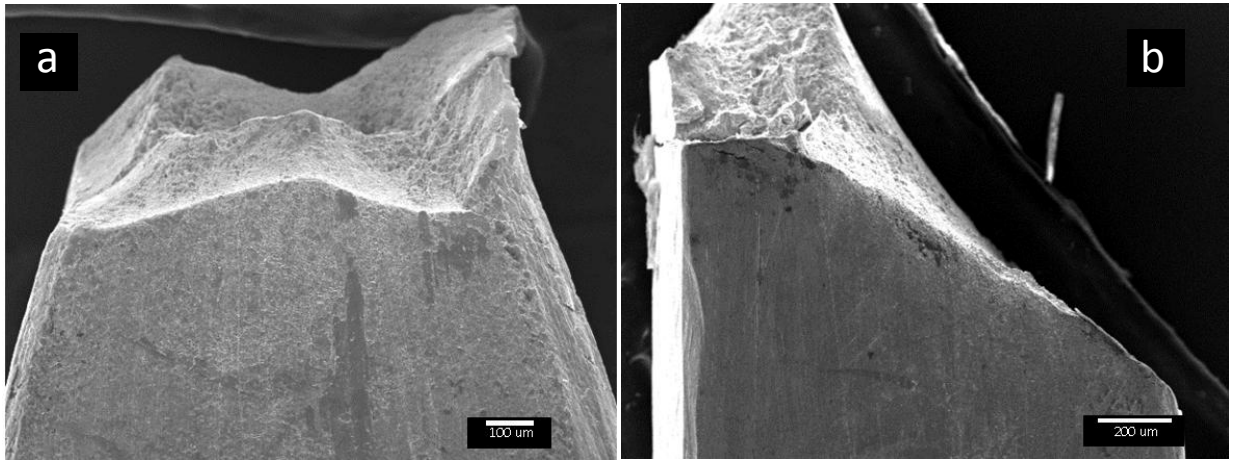

Fig. 15. SEM images of MS1500 after LIST simultaneous with hydrogen charging in 0.1 M NaOH at a potential of -1700 $mV_{Hg/HgO}$ (-1602 mV_{SHE}) and at an applied stress rate of (a) 0.80 and (b) 0.080 MPa s^{-1}. Fig. 15a shows the ductile cup-cone fracture, whilst Fig. 15b shows a brittle shear fracture.

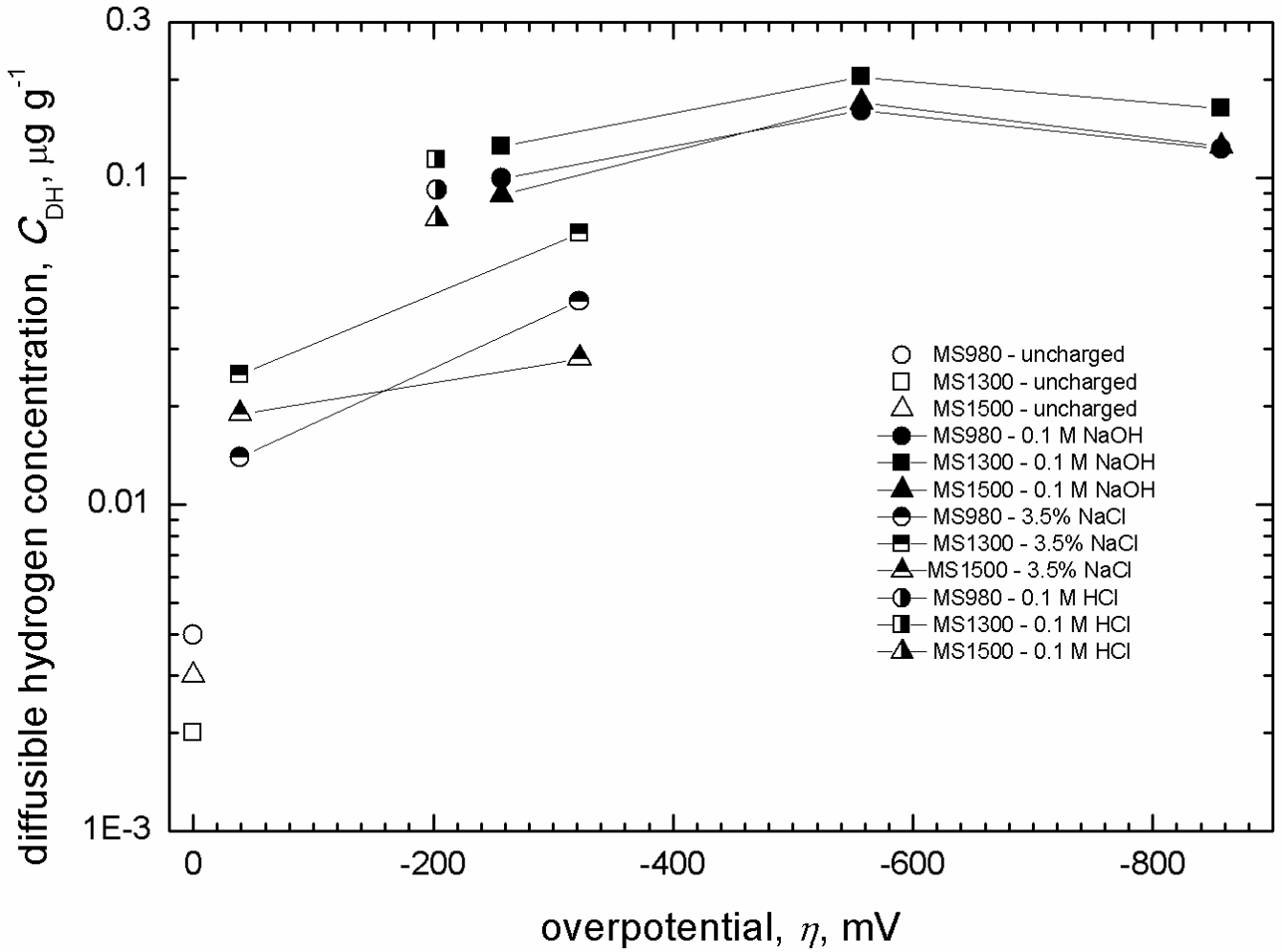

Fig. 16. The plot of diffusible hydrogen vs overpotential for MS980, MS1300 and MS1500.

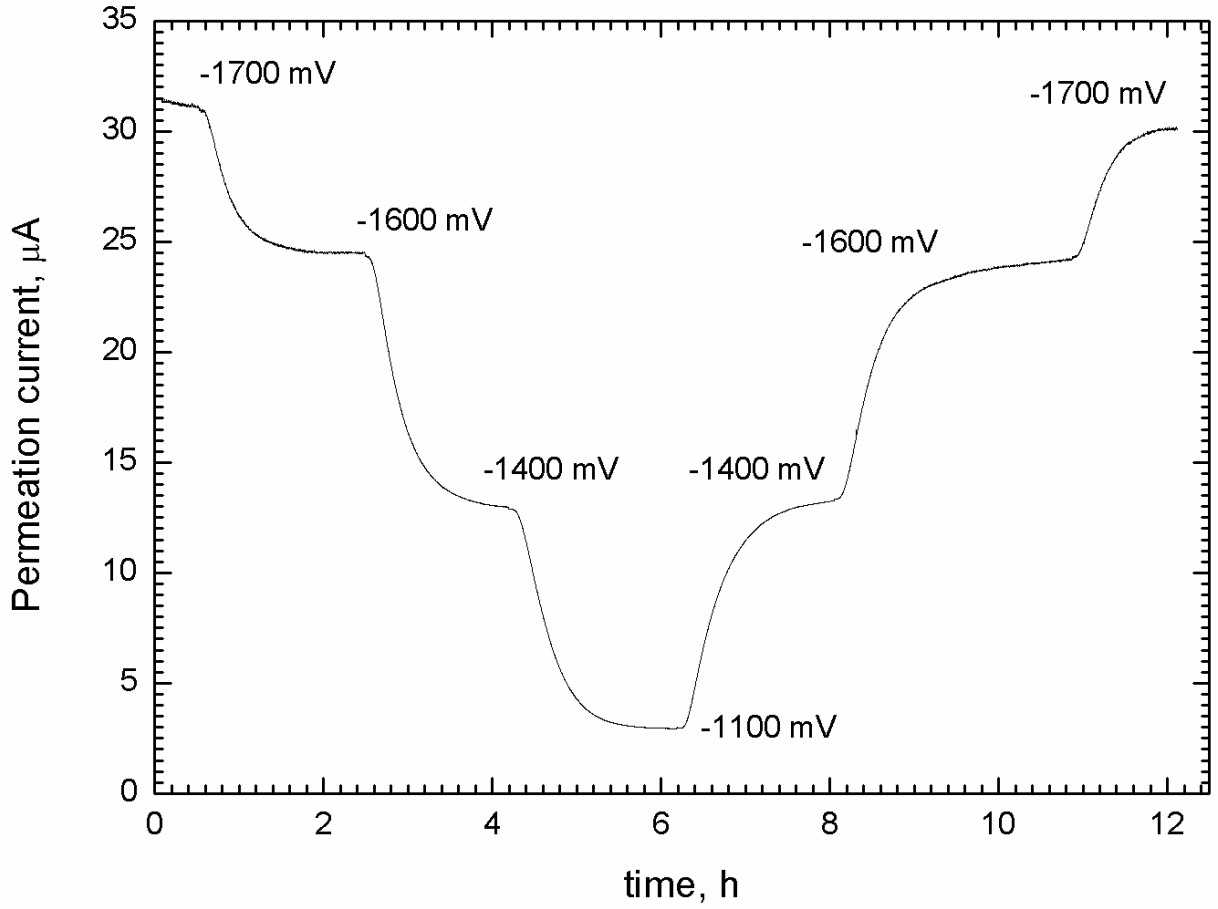

Fig. 17. Plot of permeation current vs time showing the typical transient loop to determine the effective diffusion coefficient of hydrogen in the steels. (Sample: MS1300)

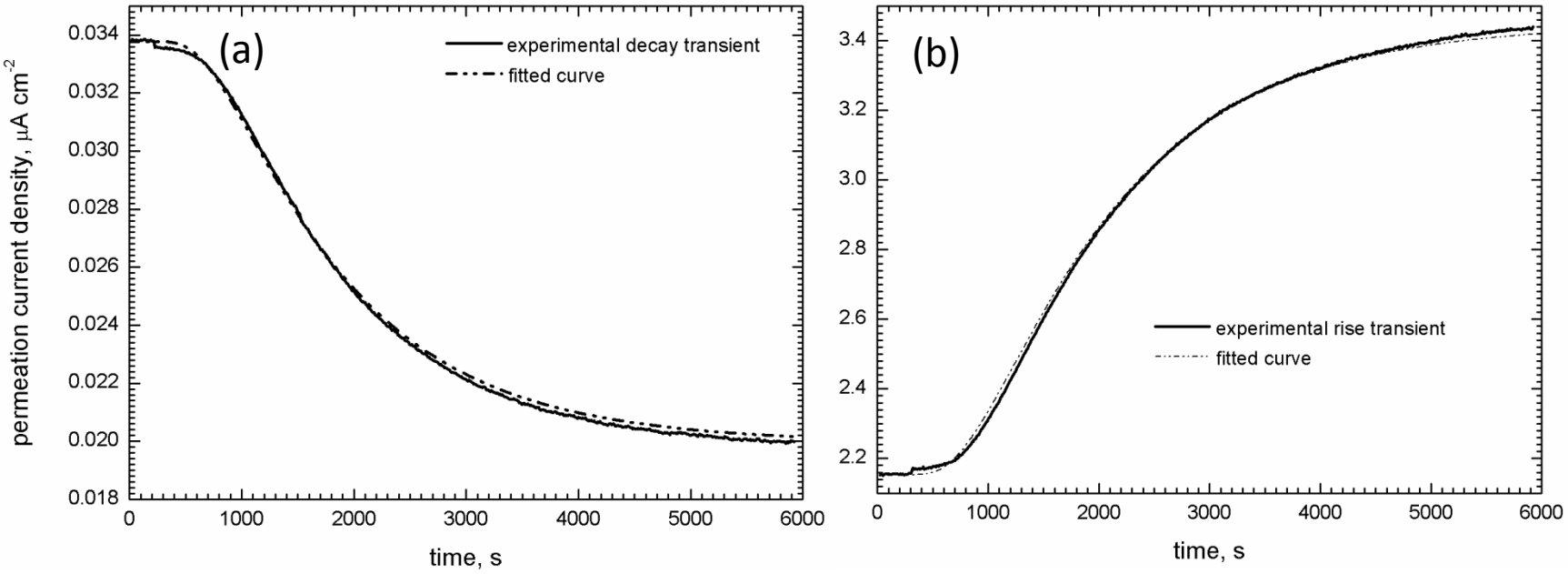

Fig. 18. An example of the theoretical curve fitted over the (a) decay (-1700 to -1600 $mV_{Hg/HgO}$ and (b) build-up transients (1600 to -1700 $mV_{Hg/HgO}$). (Sample MS1500)

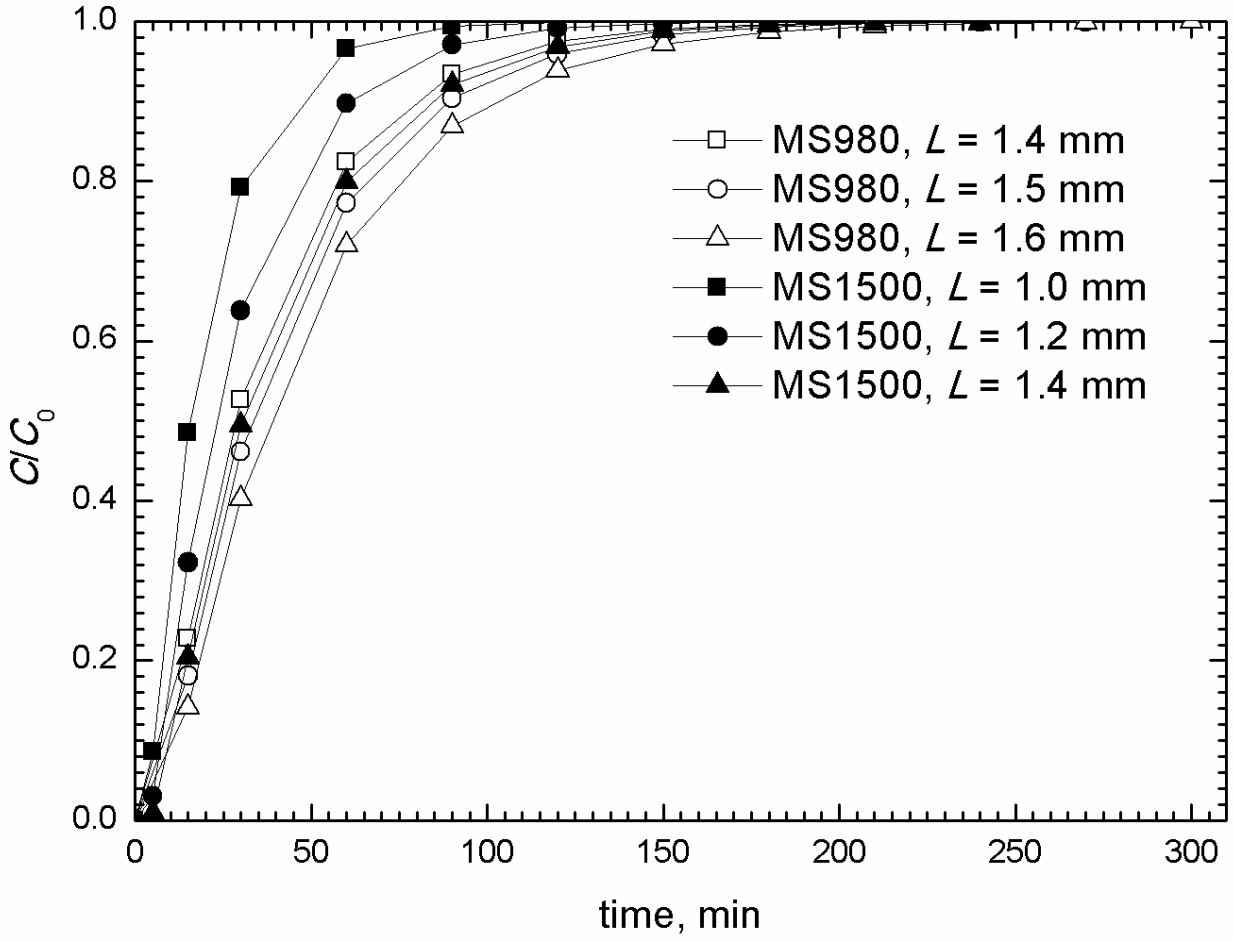

Fig. 19. Plot *C*/*C*o at the center of MS980 and MS1500 as a function of charging time and thickness, *L*.

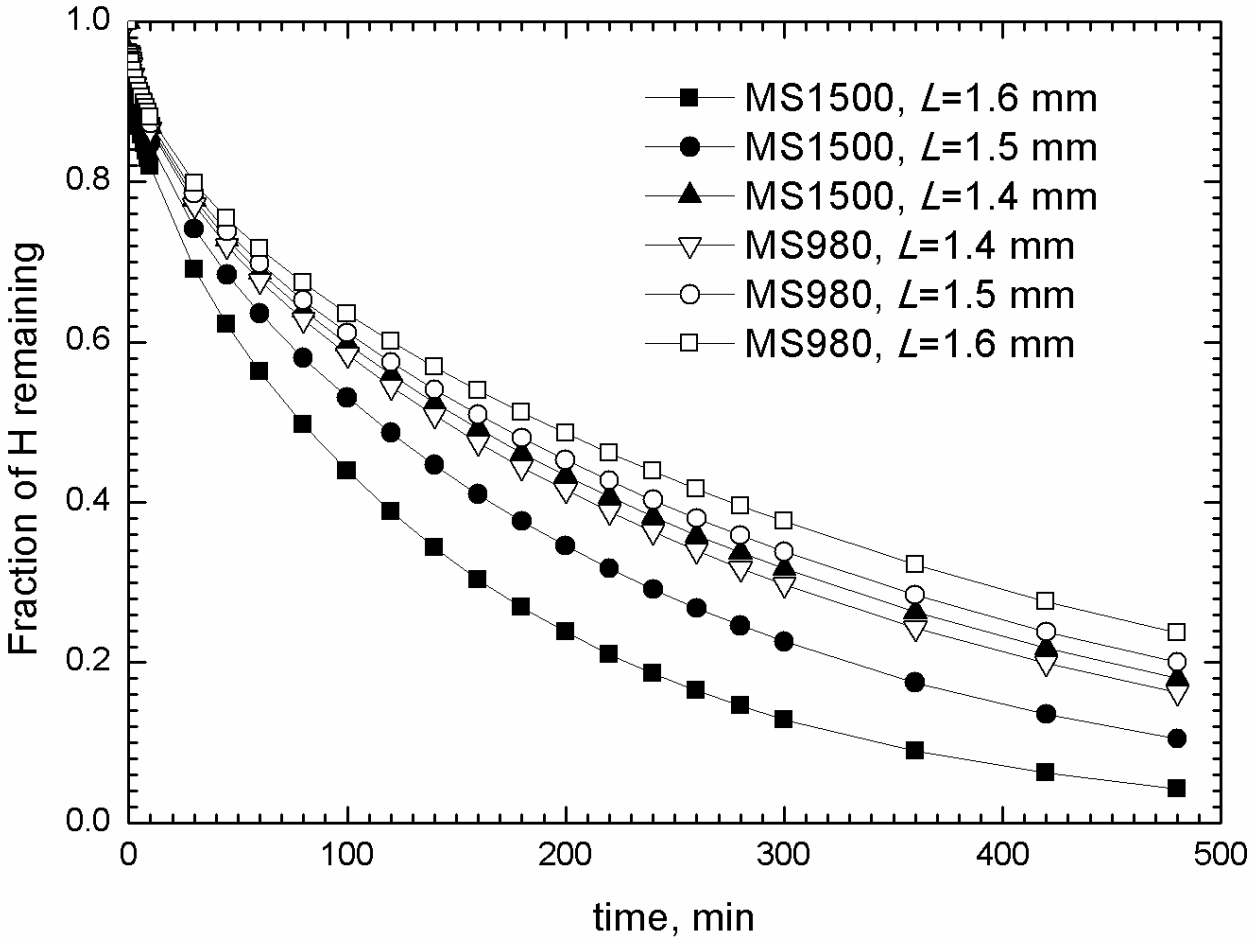

Fig. 20. Plot showing the fraction of hydrogen remaining in MS980 and MS1500, as a function of time and thickness, *L*.

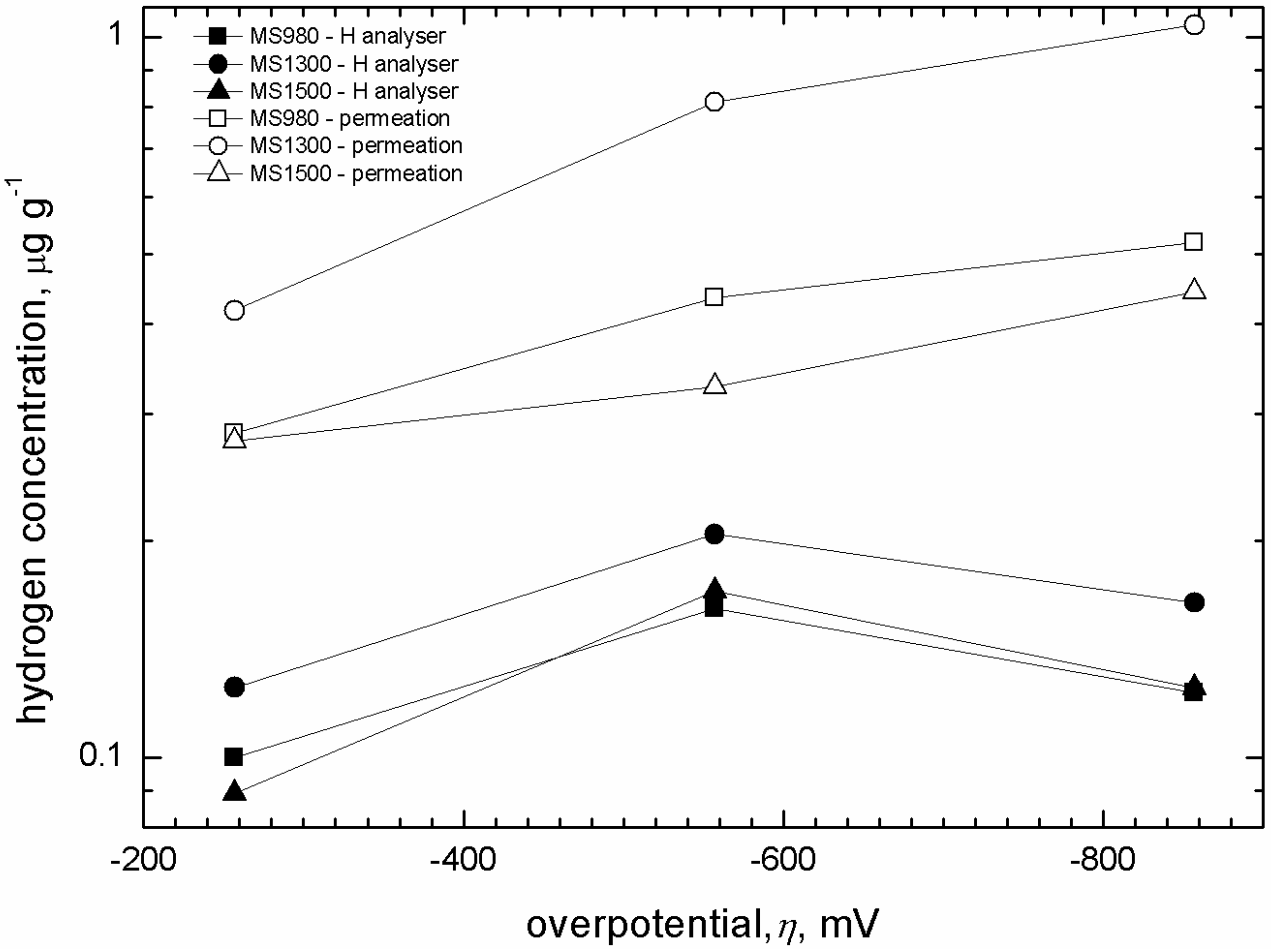

Fig. 21. Plot comparing the hydrogen concentration measured using the diffusible hydrogen analyser and the permeation experiment in MS980, MS1300 and MS1500.

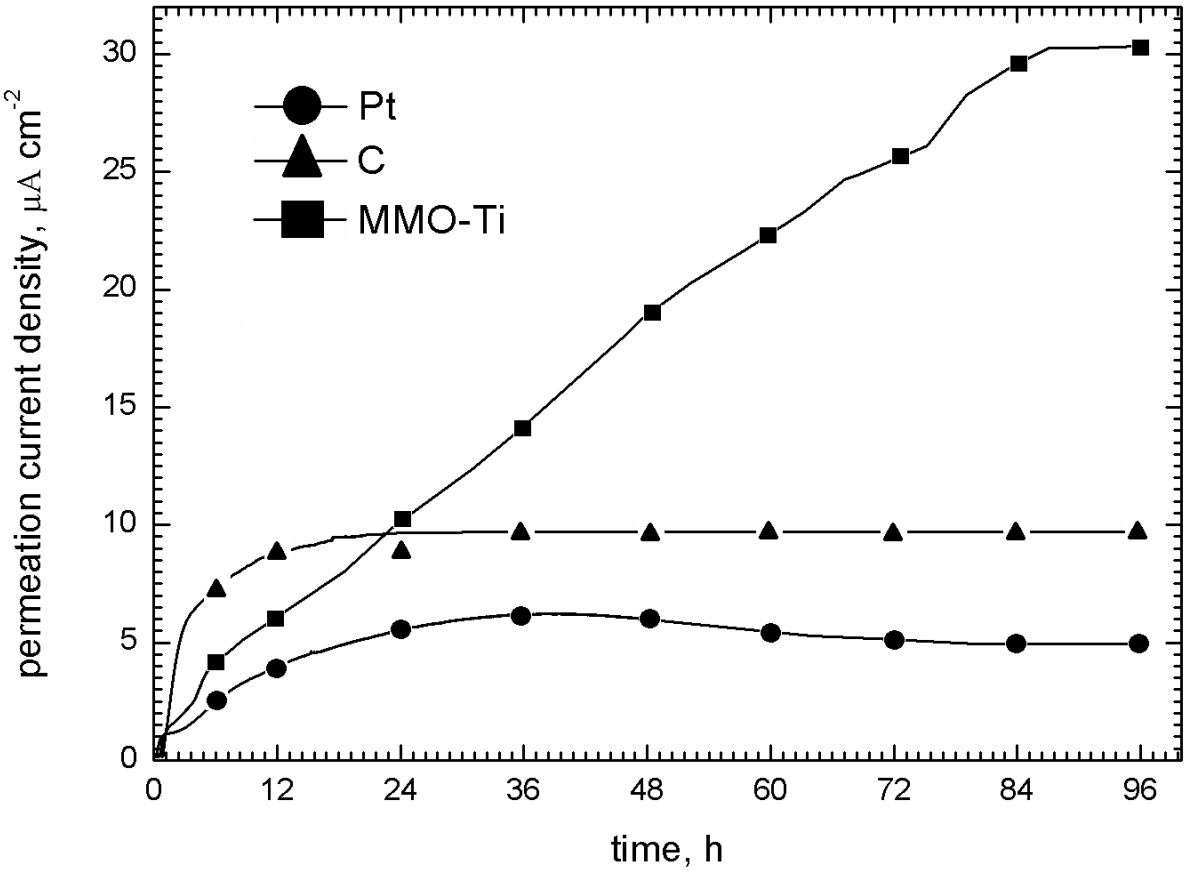

Fig. A1. Comparison of the permeation current density in MS1500 as a function of time during cathodic charging in 0.1 M NaOH at -1700 $mV_{Hg/HgO}$ (-1602 mV_{SHE}) on the input side, carried out under identical conditions, except that the counter-electrode used was Pt, C, or a MMO-Ti counter electrode .

Table 1. Chemical composition (in wt %) and mechanical properties of the MS-AHSS.

Specimen designation	Commercial designation	C	Si	Mn	S	P	Al	Nb	Ti	Cr	Yield stress, MPa	Tensile stress, MPa	Elongation at fracture, e_f	e_f, %
MS980	MS 800/980	0.12	0.37	1.63	0.01	0.01	0.03	0.02	0.04	0.02	883	1070	7.9	5
MS1180	MS 950/1180	0.15	0.37	1.64	0.01	0.01	0.03	0.01	0.03	0.02	1176	1355	5.3	3
MS1300	MS 1030/1300	0.15	0.39	1.67	0.01	0.01	0.04	0.02	0.03	0.01	1185	1380	3.5	2.5
MS1500	MS 1200/1500	0.19	0.36	1.51	0.01	0.01	0.04	0.02	0.03	0.02	1361	1667	3.9	2.9

Table 2. LIST results for MS-AHSS in air or in 3.5 wt% NaCl solution. E_{Zn} potential equals 950 $mV_{Ag/AgCl}$ (-752 mV_{SHE}). In the experiments in solution, the specimen was exposed to the solution for 24 h at 20% yield stress immediately prior to the commencement of the test. In all cases the fractography was ductile, with necking and a cup-cone fracture, with MVC dimples present on the fracture surface, unless otherwise noted. n/a is not applicable. The test with MS1500-Ezn-3-C used a carbon (graphite) counter electrode. All other tests at at the zinc potential, E_{Zn}, were carried out with a platinum (Pt) counter electrode.

Specimen designation	Environment	Potential, $V_{Ag/AgCl}$	Applied stress rate, MPA s^{-1}	Threshold or Yield stress σ_{TH}, MPa (±5)	Fracture stress, UTS, σ_F, MPa (±2)	Reduction in area, R_A, %	Hydrogen embrittlement index, I	Remarks
MS980-A-30	Air	n/a	0.064	900	1112	72	n/a	
MS980-Eo-30	NaCl	E_{corr}	0.064	880	1088	72	0	
MS980-Ezn-30	NaCl	E_{Zn}	0.064	900	1094	71	0	
MS980-Eo-3	NaCl	E_{corr}	0.0064	840	1050	71	0	
MS980-Ezn-3	NaCl	E_{Zn}	0.0064	885	1058	73	0	
MS1180-A-30	Air	n/a	0.054	1160	1348	68	n/a	
MS1180-Eo-30	NaCl	E_{corr}	0.054	1150	1348	67	0	
MS1180-Ezn-30	NaCl	E_{Zn}	0.054	1120	1344	67	0	
MS1180-Eo-3	NaCl	E_{corr}	0.0054	1140	1342	69	0	
MS1180-Ezn-3	NaCl	E_{Zn}	0.0054	1120	1340	67.5	0	
MS1300-A-30	Air	n/a	0.080	1170	1380	68	n/a	
MS1300-Eo-30	NaCl	E_{corr}	0.080	1090	1314	69	0	
MS1300-Ezn-30	NaCl	E_{Zn}	0.080	1100	1318	68	0	
MS1300-Eo-3	NaCl	E_{corr}	0.0080	1080	1302	66	3	
MS1300-Ezn-3	NaCl	E_{Zn}	0.0080	1085	1290	66	3	
MS1500-A-30	Air	n/a	0.080	1345	1598	62	n/a	
MS1500-Eo-30	NaCl	E_{corr}	0.080	1330	1592	60	3	
MS1500-Ezn-30	NaCl	E_{Zn}	0.080	1320	1590	60	3	
MS1500-Eo-3	NaCl	E_{corr}	0.0080	1320	1580	60	3	
MS1500-Ezn-3	NaCl	E_{Zn}	0.0080	1305	1564	56	10	Ductile; necking and cup-cone fracture. MVC dimples on the fracture surface; long crack across the surface parallel to the broad transverse side.
MS1500-Ezn-3-C	NaCl	E_{Zn}	0.0080	1330	1462	29	47	Shear fracture with some necking. Crack initiation was from the specimen edge, where there were regions of brittle intergranular fracture.

Table 3. LIST results for MS-AHSS in air or in 0.1M HCl. In the experiments in solution, the specimen was exposed to the solution for 24 h at 25% yield stress, immediately prior to the test. The threshold / yield stress and the fracture stress values are engineering stresses, based on the original specimen cross-section area. This includes the specimens subjected to crevice corrosion. For the crevice corrosion specimens, the average fracture stress was 1280 MPa and 1720 MPa for MS980 and MS1500 for the fracture stress calculated based on the remaining ligament area before fracture. *The potential drop curve did not indicate the presence of a yield or threshold stress.

Specimen designation	Environment	Potential, $V_{Ag/AgCl}$	Applied stress rate, MPA s^{-1}	Threshold / Yield stress σ_{TH}, MPa (±5)	Fracture stress, UTS, σ_F, MPa (±2)	Reduction in area, R_A, %	Hydrogen embrittlement index, I	Remarks
MS980-A-30	Air	n/a	0.064	900	1112	72	n/a	Ductile; necking and cup-cone fracture evident. MVC dimples present at fracture surface.
MS980-HCl-3-UC1	HCl	E_{corr}	0.0064	810	970	42	42	Cup and cone; small amount of necking; fine features unresolved due to oxide layer
MS980-HCl-3-UC2	HCl	E_{corr}	0.0064	815	964	31	57	Shear fracture; some indications of yielding
MS980-HCl-3-C1	HCl	E_{corr}	0.0080	*	708	8	89	The fracture surface was difficult to analyse due to excessive oxidation.
MS980-HCl-3-C2	HCl	E_{corr}	0.0064	*	678	8	89	Shear fracture in the remaining area (1.166 mm^2); shear MVC dimples at crack propagation zone.
MS1500-A-30	Air	n/a	0.080	1340	1580	63	n/a	Ductile; necking and cup-cone fracture evident. MVC dimples present at fracture surface.
MS1500-HCl-3-UC1	HCl	E_{corr}	0.0080	1300	1502	8	87	Shear fracture; some necking; fine features unresolved due to metal layer
MS1500-HCl-3-UC2	HCl	E_{corr}	0.0080	1310	1484	10	84	Shear fracture; some necking
MS980-HCl-3-C1	HCl	E_{corr}	0.0080	*	820	8	87	The fracture surface was difficult to analyse due to the presence of metal layer plated out from solution.
MS1500-HCl-3-C2	HCl	E_{corr}	0.0080	*	806	8	87	Shear fracture in the remaining area (0.758 mm^2); quasi cleavage fracture in crack nucleation zone; shear MVC dimples at the crack propagation region; secondary crack near crack nucleation zone.

Table 4. LIST results for MS1300 and MS1500 tested (i) in air (uncharged/air), (ii) in air essentially immediately after hydrogen charging in 0.1M NaOH at an applied potential of -1700 $mV_{Hg/HgO}$ (-1602 mV_{SHE}) for 24 h at 20% yield stress (NaOH/Air, specimen designation includes 10 min), (iii) in air 24 h after hydrogen charging in 0.1M NaOH at an applied potential of -1700 $mV_{Hg/HgO}$ for 24 h at 20% yield stress (NaOH/Air, specimen designation includes 24H), and (iv) in 0.1M NaOH at an applied potential of -1700 $mV_{Hg/HgO}$, after hydrogen charging in 0.1M NaOH at an applied potential of -1700 $mV_{Hg/HgO}$ for 24 h at 20% yield stress (NaOH/ NaOH). NaOH/Air means that the sample was charged in 0.1M NaOH solution and tested in air. NaOH/ NaOH means that the sample was charged in the 0.1M NaOH solution and tested in the 0.1M NaOH solution. All the hydrogen charging involved a Pt counter electrode. Unless otherwise noted in "Remarks", the fractures were ductile, with necking and cup-cone fracture, with MVC dimples present on the fracture surface. n/a is not applicable.

Specimen designation	Charging / test environment	Potential, $V_{Hg/HgO}$	Applied stress rate, MPA s^{-1}	Threshold / Yield stress σ_{TH}, MPa (±5)	Fracture stress, UTS, σ_f, MPa (±2)	Reduction in area, R_A, %	Hydrogen embrittlement index, I	Remarks
MS1300-A-UTM	Uncharged/Air	n/a	50	1140	1366	68	n/a	
MS1300-A-30	Uncharged/Air	n/a	0.080	1170	1380	68	n/a	
MS1300-10min-UTM	NaOH/Air	-1.700	50	1130	1350	65	4	
MS1300-10min-300	NaOH/Air	-1.700	0.80	1150	1362	68	0	
MS1300-10min-30	NaOH/Air	-1.700	0.080	1135	1306	70	0	
MS1300-24H-300	NaOH/Air	-1.700	0.80	1140	1350	68	0	
MS1300-24H-30	NaOH/Air	-1.700	0.80	1130	1302	69	0	
MS1300-24H-UTM	NaOH/Air	-1700	50	1140	1370	69	0	
MS1300-H1.7-300	NaOH/NaOH	-1700	0.80	1120	1360	69	0	
MS1300-H1.7-30	NaOH/NaOH	-1700	0.080	1020	1330	34	50	Mixed ductile and shear fracture. Some signs of necking. Brittle crack initiation zone, ductile shear zone.
MS1500-A-UTM	Uncharged/Air	n/a	50	1340	1580	63	n/a	
MS1500-A-30	Uncharged/Air	n/a	0.080	1345	1598	62	n/a	
MS1500-10min-UTM	NaOH/Air	-1.700	50	1330	1550	58	8	
MS1500-10min-300	NaOH/Air	-1.700	0.80	1340	1588	60	5	
MS1500-10min-30	NaOH/Air	-1.700	0.080	1350	1586	60	5	
MS1500-H1.7-300	NaOH/NaOH	-1700	0.80	1315	1580	60	5	
MS1500-H1.7-30	NaOH/NaOH	-1700	0.080	1280	1510	7	89	Complete shear fracture. Necking was absent. Brittle crack initiation zone consisted of intergranular fracture, ductile shear crack propagation zone.

Table 5. Diffusible hydrogen content of MS980, MS1300, and MS1500 charged under the conditions indicated. For cathodic charging, a Pt counter electrode was used.

	Diffusible hydrogen, μg g^{-1}						
Charging conditions	Uncharged	3.5% NaCl		0.1 M HCl	0.1 M NaOH		
		E_{Zn}	E_o	E_o	-1700 $mV_{Hg/HgO}$ (-1602 mV_{SHE})	-1400 $mV_{Hg/HgO}$ (-1302 mV_{SHE})	-1300 $mV_{Hg/HgO}$ (-1002 mV_{SHE})
Overpotential, mV	0	-322	-39	-203	-857	-557	-257
MS980	0.004	0.042	0.014	0.092	0.123	0.161	0.1
MS1300	0.002	0.068	0.025	0.114	0.163	0.204	0.125
MS1500	0.003	0.028	0.019	0.075	0.125	0.17	0.089

Table 6. Table of D_{eff} and C_H of MS980, MS300 and MS1500 obtained from decay and build-up transients in the permeation experiments.

Steel	Applied potential, $mV_{Hg/HgO}$	η, mV	i_{∞}, $\mu A\ cm^{-2}$	D_{eff}, $cm\ s^{-1}$	C_H, $ug\ g^{-1}$
MS980	Start at -1700	-857	3.11		0.518
	-1600 (decay)	-757	2.61	11.7×10^{-7}	0.435
	-1400 (decay)	-557	1.69	10.7×10^{-7}	0.282
	-1100 (decay)	-257	0.63	10.5×10^{-7}	0.099
	-1400 (rise)	-557	1.95	10.2×10^{-7}	0.326
	-1600 (rise)	-757	2.91	10.7×10^{-7}	0.484
	-1700 (rise)	-857	3.25	11.3×10^{-7}	0.541
				Ave : 10.9×10^{-7}	
MS1300	Start at -1700	-857	8.61		1.039
	-1600 (decay)	-757	6.72	11.2×10^{-7}	0.812
	-1400 (decay)	-557	3.46	11.5×10^{-7}	0.417
	-1100 (decay)	-257	6.08	10.9×10^{-7}	0.073
	-1400 (rise)	-557	3.52	10.2×10^{-7}	0.426
	-1600 (rise)	-757	6.53	10.4×10^{-7}	0.789
	-1700 (rise)	-857	8.31	13.8×10^{-7}	1.003
				Ave: 11.3×10^{-7}	
MS1500	Start at -1700	-857	4.40		0.443
	-1600 (decay)	-757	3.36	11.6×10^{-7}	0.327
	-1400 (decay)	-557	1.97	10.2×10^{-7}	0.275
	-1100 (decay)	-257	0.46	10.8×10^{-7}	0.053
	-1400 (rise)	-557	2.15	9.10×10^{-7}	0.259
	-1600 (rise)	-757	3.45	9.60×10^{-7}	0.380
	-1700 (rise)	-857	4.23	9.40×10^{-7}	0.545
				Ave: 10.2×10^{-7}	

Table A1. Values for the measured stead-state permeation current density, the effective diffusion coefficient, D_{eff}, and the hydrogen concentration, C_H, in the steel on the input side of the MS1500 steel permeation specimen from a sequence of permeation decay transients after long term (4 d) cathodic charging in 0.1 M NaOH at -1700 $mV_{Hg/HgO}$ (-1602 mV_{SHE}) on the input side, carried out under identical conditions, except that the counter-electrode used was Pt, C, or a MMO-Ti counter electrode.

Counter electrode material	Applied potential, $mV_{Hg/HgO}$	η, mV	i_{∞}, $\mu A\ cm^{-2}$	D_{eff}, $cm\ s^{-1}$	C_H, $ug\ g^{-1}$
Pt	Start at -1700	-857	4.40		0.443
	decay to -1600	-757	3.36	11.6×10^{-7}	0.327
	decay to -1400	-557	1.97	10.2×10^{-7}	0.275
	decay to -1100	-257	0.46	10.8×10^{-7}	0.053
				Ave: 10.2×10^{-7}	
C	Start at -1700	-857	9.42		1.306
	-1600 (decay)	-757	6.57	9.4×10^{-7}	0.910
	-1400 (decay)	-557	2.91	9.8×10^{-7}	0.404
	-1100 (decay)	-257	1.22	9.5×10^{-7}	0.169
				Ave: 9.6×10^{-7}	
MMO-Ti	Start at -1700	-857	31.0		2.363
	-1600 (decay)	-757	23.1	17.4×10^{-7}	1.758
	-1400 (decay)	-557	8.23	15.7×10^{-7}	0.627
	-1100 (decay)	-257	1.08	10.0×10^{-7}	0.082
				Ave: 14.4×10^{-7}	

Table A2. Composition of the electrolyte in the counter electrode compartment at the start of precharging at cathodic charging in 0.1 M NaOH at -1700 $mV_{Hg/HgO}$ (-1602 mV_{SHE}) on the input side (0 h), after 96 h, and at the end of the cathodic charging (120 h).

Sample Designation	Element concentration, mg/L													
	Ir	Ru	Ta	Ti	Al	Pb	Fe	Ca	P	S	Si	Na	K	Zn
0 h	0.023	0.004	0.021	0.008	0.264	0.010	0.037	0.010	0.087	0.149	8.799	2291	0.676	0.002
96 h	0.296	0.014	0.081	0.091	0.602	0.012	0.011	0.035	0.105	0.368	21.514	2296	18.947	0.017
120 h	0.087	0.010	0.059	0.019	0.792	0.017	0.017	0.030	0.116	0.277	25.215	2357	40.592	0.029